

Supporting Information:

Bayesian data analysis reveals no preference for cardinal Tafel slopes in CO₂ reduction electrocatalysis

Aditya M. Limaye,[†] Joy S. Zeng,[†] Adam P. Willard,^{*,‡} and Karthish Manthiram^{*,†}

[†]*Department of Chemical Engineering, MIT, Cambridge, MA*

[‡]*Department of Chemistry, MIT, Cambridge, MA*

E-mail: awillard@mit.edu; karthish@mit.edu

1 Supplementary Discussion

2 Literature Analysis

3 Dataset Organization

4 In this study, we manually digitized Tafel data included in several different papers from
5 the electrochemical CO₂ reduction literature. Often, a single paper may report multiple
6 sets of Tafel data, possibly with many traces in the same figure. Each distinct paper that
7 reports (possibly multiple) Tafel data(sets) receives a unique three-digit identifier, which will
8 be referred to as PaperID. Note that PaperIDs are *not* guaranteed to be consecutive, and
9 some numbers are skipped. Within each paper, each dataset receives a separate three-digit

10 identifier (unique within the same `PaperID`), which will be referred to as `SetID`. A single
11 Tafel dataset in our study, then, is uniquely identified by the tuple (`PaperID`, `SetID`).

12 Our entire zipped dataset is organized into a hierarchical directory structure, with each
13 directory named according to the `PaperID` identifier. Each individual paper directory con-
14 tains several files. First, we include files with names of the form `figure*.png`, which are
15 raw Portable Network Graphics (PNG) images of the paper figures, screenshotted manually
16 from PDF copies of the papers. A few paper directories have multiple figure screenshots, and
17 they are named according to `figure1.png`, `figure2.png`, etc. Directories also include raw
18 data files with names of the form `dat_<SetID>.txt`, which contain raw $x;y$ data taken from
19 manually digitizing the figure. Associated with each raw data file is a separate metadata
20 file with a name of the form `metadata_<SetID>.txt`. The metadata files contain key-value
21 pairs stored in the YAML Ain't Markup Language (YAML) format, and contain several
22 pieces of information required for processing the raw $x;y$ data. YAML parsers are avail-
23 able in several programming languages, and the official YAML standard is documented at
24 <https://yaml.org/>.

25 **Metadata Tags**

26 Tags in a metadata file are associated with YAML keys, and their associated values have
27 several types. The types of the values, as well as the information they carry, are documented
28 in Table 1. Note that for CO_2 reduction catalysis, more negative applied electrochemical
29 potentials correspond to more positive overpotentials. Studies in the literature report ei-
30 ther the applied electrochemical potential or the overpotential on their voltage axis. The
31 `v_reversed` tag contains the information required to properly orient the voltage data in the
32 direction of increasing overpotential for each dataset.

Supplementary Table 1: Table describing the types and meanings of the key-value pairs in the metadata files associated with each Tafel dataset.

Tag Name	Value Type	Value Meaning
<code>xdat</code>	Enum[<code>'current'</code> , <code>'voltage'</code>]	Indicates which data is reported on the x axis.
<code>xunit</code>	String	String describing units of measurement for the x axis data, for example <code>mV</code> or <code>mA/cm2</code> .
<code>xlog</code>	Bool	Indicates whether the x axis data is reported on a logarithmic scale.
<code>ydat</code>	Enum[<code>'current'</code> , <code>'voltage'</code>]	Indicates which data is reported on the y axis.
<code>yunit</code>	String	String describing units of measurement for the y axis data, for example <code>mV</code> or <code>mA/cm2</code> .
<code>ylog</code>	Bool	Indicates whether the y axis data is reported on a logarithmic scale.
<code>rval</code>	Float	Reported Tafel slope value.
<code>rerr</code>	Union[Float, None]	Error in reported Tafel slope value, if reported. If not reported, then <code>None</code> .
<code>runit</code>	String	String describing units of measurement for the x axis data, for example <code>mV/dec</code> .
<code>v_reversed</code>	Bool	If <code>false</code> , then the voltage data increases in value with increasing direction of the axis. If <code>true</code> , then the voltage data decreases in value with decreasing direction of the axis.
<code>i_reversed</code>	Bool	If <code>false</code> , then the current data increases in value with increasing direction of the axis. If <code>true</code> , then the current data decreases in value with decreasing direction of the axis.
<code>cat_tags</code>	List[String]	A list of tags describing the catalyst material. For example, a CuO catalyst would get the tags [<code>'Cu'</code> , <code>'O'</code>].

33 **Analyzed Papers**

34 Table 2 documents the literature sources of all Tafel datasets analyzed in this study.

Supplementary Table 2: Provenance of all Tafel datasets analyzed in this study. The PaperID defines the unique identifier assigned to the paper in the zipped dataset.

PaperID	Data Location	Document Object Identifier (DOI)
000	Figure 5	10.1021/ja5065284 ¹
002	Figure 4	10.1021/ja309317u ²
004	Figure 4	10.1246/bcsj.68.1889 ³
005	Figure 4	10.1002/anie.201604654 ⁴
009	Figure 5B	10.1021/acsnano.5b01079 ⁵
010	Figure 4B	10.1002/anie.201713003 ⁶
011	Figure 1C	10.1021/jacs.7b09074 ⁷
012	SI Figure 8	10.1002/anie.201900499 ⁸
014	Figure 10	10.1002/sm11.201701809 ⁹
015	Figure 6D	10.1088/1361-6528/aa8f6f ¹⁰
016	Figure 7A	10.1021/jacs.5b02975 ¹¹
017	SI Figure 6	10.1002/sm11.201602158 ¹²
021	Figure 5C	10.1002/celc.201700517 ¹³
022	Figure 3A, 3C	10.1002/cssc.201600202 ¹⁴
023	Figure 4A	10.1021/ja501923g ¹⁵
024	Figure 4B	10.1021/acsenerylett.8b00472 ¹⁶
025	SI Figure 12	10.1021/ja4113885 ¹⁷
026	Figure 2D	10.1016/j.elecom.2016.05.003 ¹⁸
027	Figure 3A, 3C	10.1021/ja2108799 ¹⁹
028	Figure 7A	10.1021/acs.jpcc.7b01586 ²⁰
029	SI Figure 13	10.1021/acscatal.7b00707 ²¹
031	Figure 7	10.1016/j.electacta.2016.03.182 ²²

032	Figure 8	10.1016/j.jcou.2017.05.024 ²³
033	Figure 2D	10.1002/cssc.201902859 ²⁴
035	Figure 4	10.1021/acscami.8b03461 ²⁵
036	SI Figure 8	10.1021/acscami.7b10421 ²⁶
039	Figure 3A	10.1002/asia.201800946 ²⁷
040	Figure 7	10.1002/cssc.201802409 ²⁸
042	SI Figure 4	10.1021/acsaem.8b00356 ²⁹
043	SI Figure 14	10.1021/acs.jpcc.8b06234 ³⁰
045	SI Figure 13	10.1021/acsaem.8b02048 ³¹
048	Figure 6C	10.1002/celc.201801132 ³²
049	Figure 4C	10.1002/adma.201706194 ³³
050	Figure 3	10.1038/ncomms4242 ³⁴
051	Figure 4	10.1021/acscatal.5b01235 ³⁵
052	Figure 4E	10.1002/aenm.201701456 ³⁶
053	Figure 3F	10.1016/j.chempr.2017.08.002 ³⁷
054	Figure 4C	10.1002/anie.201608279 ³⁸
055	Figure 7A	10.1016/j.apcatb.2018.01.001 ³⁹
056	Figure 4	10.1021/ja3010978 ⁴⁰
057	Figure 2C	10.1016/j.apcatb.2018.09.025 ⁴¹
058	Figure 5D	10.1021/jacs.6b10435 ⁴²
059	Figure 6	10.1021/jacs.6b12217 ⁴³
060	Figure 2F	10.1002/ange.201805696 ⁴⁴
061	Figure 6	10.20964/2017.03.72 ⁴⁵
062	Figure 3B	10.1002/cssc.201702229 ⁴⁶
063	Figure 3D	10.1002/aenm.201801536 ⁴⁷
064	Figure 4A	10.1016/j.jcis.2018.09.036 ⁴⁸
065	Figure 7	10.1016/j.nanoen.2018.03.023 ⁴⁹

066	Figure 3D	10.1021/jacs.7b12506 ⁵⁰
067	Figure 2D	10.1021/acscatal.5b00922 ⁵¹
068	Figure 3F	10.1021/acsnano.7b03029 ⁵²
069	Figure 4D	10.1021/acscatal.7b03449 ⁵³
070	Figure 8	10.1016/j.apsusc.2016.10.017 ⁵⁴
071	Figure 3	10.1002/anie.201802055 ⁵⁵
072	Figure 6A	10.1016/j.electacta.2018.04.047 ⁵⁶
074	Figure 2G	10.1021/jacs.5b08212 ⁵⁷
076	Figure 3A	10.1002/anie.201809255 ⁵⁸
077	Figure 4A	10.1002/anie.201711255 ⁵⁹
078	Figure 3G	10.1016/j.nanoen.2018.09.053 ⁶⁰
080	Figure 2H	10.1002/anie.201800367 ⁶¹
081	Figure 7	10.1016/j.cej.2016.02.084 ⁶²
083	Figure 2B	10.1016/j.apcatb.2017.06.032 ⁶³
084	Figure 2E	10.1016/j.jcat.2018.05.005 ⁶⁴
085	Figure 3E	10.1002/anie.201803873 ⁶⁵
086	Figure 3C	10.1002/anie.201806043 ⁶⁶
087	Figure 4D	10.1016/j.electacta.2018.09.080 ⁶⁷
088	Figure 5	10.1023/B:JACH.0000003866.85015.b6 ⁶⁸
089	Figure 6	10.1021/jp9822945 ⁶⁹
090	Figure 5C	10.1002/smll.201704049 ⁷⁰
091	Figure 5D	10.1016/j.nanoen.2016.11.004 ⁷¹
092	Figure 5B	10.1002/anie.201701104 ⁷²
093	Figure 3A	10.1021/jacs.6b12103 ⁷³
094	Figure 4A	10.1002/anie.201903613 ⁷⁴
095	SI Figure 8C	10.1002/anie.201900499 ⁸
096	Figure 2B	10.1002/adfm.201800499 ⁷⁵

097	SI Figure 6	10.1016/j.cattod.2015.05.017 ⁷⁶
098	Figure 4C	10.1021/acscami.7b16164 ⁷⁷
099	Figure 3	10.1002/sml1.201703314 ⁷⁸
100	Figure 4A	10.1016/j.apcatb.2018.08.075 ⁷⁹
101	Figure 4D	10.1073/pnas.1711493114 ⁸⁰
102	Figure 5B	10.1002/cssc.201800925 ⁸¹
103	Figure 1C	10.1021/acscatal.5b02424 ⁸²
104	Figure 3F	10.1021/acscenergylett.8b00519 ⁸³
105	Figure 4B	10.1002/anie.201612194 ⁸⁴
106	Figure 3C	10.1002/anie.201703720 ⁸⁵
108	SI Figure 4	10.1021/acs.nanolett.5b04123 ⁸⁶
109	Figure 3F	10.1002/anie.201901575 ⁸⁷
110	Figure 3D	10.1016/j.electacta.2018.12.116 ⁸⁸
111	Figure 5A	10.1021/acscatal.8b01022 ⁸⁹
112	Figure 3	10.1002/cssc.201701673 ⁹⁰
113	Figure 2D	10.1002/aenm.201900276 ⁹¹
114	Figure 2D	10.1021/acscenergylett.8b01286 ⁹²
115	Figure 2D	10.1002/anie.201712221 ⁹³
116	Figure 2D	10.1002/anie.201807571 ⁹⁴
117	Figure 3A	10.1021/acscenergylett.7b01096 ⁹⁵
118	Figure 5	10.1021/acsaem.8b01692 ⁹⁶
119	Figure 6	10.1039/C5CP03559G ⁹⁷
120	SI Figure 6	10.1126/science.aaw7515 ⁹⁸
121	Figure 10	10.1002/celc.201801036 ⁹⁹
122	Figure 5A	10.1002/adma.201705872 ¹⁰⁰
123	Figure 4C	10.1021/acscatal.8b04852 ¹⁰¹
124	Figure 2F	10.1016/j.jcou.2019.05.026 ¹⁰²

125	Figure 3D	10.1002/ange.201810538 ¹⁰³
126	Figure 3C	10.1016/j.joule.2018.11.008 ¹⁰⁴
127	Figure 1D	10.1002/aenm.201700759 ¹⁰⁵
128	Figure 5B	10.1002/celec.201700935 ¹⁰⁶
129	Figure 4B	10.1016/j.apcatb.2019.03.047 ¹⁰⁷
130	SI Figure 5B	10.1002/anie.201911995 ¹⁰⁸
131	SI Figure 12	10.1002/aenm.201702524 ¹⁰⁹
132	Figure 4C	10.1002/ange.201805256 ¹¹⁰
133	SI Figure 10	10.1002/aenm.201601103 ¹¹¹
134	Figure 2A	10.1038/s41467-018-07970-9 ¹¹²
135	Figure 2B	10.1016/j.nanoen.2019.05.003 ¹¹³
136	Figure 4	10.1039/C6TA04325A ¹¹⁴
137	Figure 2D	10.1002/celec.201800806 ¹¹⁵
138	Figure 3B	10.1002/anie.201805871 ¹¹⁶
139	Figure 4	10.1002/chem.201603359 ¹¹⁷
140	Figure 3D	10.1002/aenm.201903068 ¹¹⁸
141	Figure 3	10.1002/cssc.201501637 ¹¹⁹
142	Figure 3F	10.1002/anie.201907399 ¹²⁰
143	Figure 3E	10.1016/j.electacta.2018.08.002 ¹²¹
144	Figure 4A	10.1021/jp509967m ¹²²
145	SI Figure 8	10.1021/acs.est.5b00066 ¹²³
146	SI Figure 10	10.1021/acscatal.6b00543 ¹²⁴
147	SI Figure 39	10.1016/j.joule.2019.05.010 ¹²⁵
148	Figure 3B	10.1016/j.jcou.2019.02.007 ¹²⁶
149	Figure 4D	10.1002/cssc.201903117 ¹²⁷
150	Figure 3C	10.1002/chem.201803615 ¹²⁸
151	Figure 5D	10.1002/celec.201800104 ¹²⁹

152	Figure 4A	10.1039/C9EE00018F ¹³⁰
153	SI Figure 10	10.1016/j.joule.2018.10.015 ¹³¹
154	Figure 5	10.1002/celc.201900725 ¹³²
155	Figure 4B	10.1038/ncomms14503 ¹³³
156	Figure 2D	10.1016/j.elecom.2018.10.014 ¹³⁴
157	Figure 2C	10.1002/aenm.201803151 ¹³⁵
158	Figure 4E	10.1016/j.elecom.2019.03.017 ¹³⁶
159	Figure 4B, 4C	10.1002/cssc.201802725 ¹³⁷
160	Figure 12	10.1016/j.matchemphys.2017.02.016 ¹³⁸
161	Figure 4	10.1002/adfm.201802339 ¹³⁹
162	Figure 4D	10.1016/j.nanoen.2016.06.043 ¹⁴⁰
163	Figure 4C	10.1038/ncomms12697 ¹⁴¹
164	Figure 4F	10.1021/acssuschemeng.9b03502 ¹⁴²
165	Figure 5B	10.1039/C8TA03328E ¹⁴³
166	Figure 6C	10.1039/C7TA03005C ¹⁴⁴
167	Figure 3A	10.1002/anie.201908735 ¹⁴⁵
168	Figure 6D	10.1021/acsaem.9b02324 ¹⁴⁶
169	Figure 2C	10.1021/acs.jpcc.9b09730 ¹⁴⁷
170	Figure 3A	10.1073/pnas.1602984113 ¹⁴⁸
171	Figure 2	10.1021/acscatal.8b02181 ¹⁴⁹

35 Data Licensing

36 Code that supports the findings of this study is available under the MIT License in Zenodo
37 (<http://doi.org/10.5281/zenodo.3995021>). Data that supports the findings of this study
38 is available under CC BY 4.0 (<https://creativecommons.org/licenses/by/4.0/>) in Zen-
39 odo (<http://doi.org/10.5281/zenodo.3995021>), with the exception of the excerpted fig-
40 ures from other articles as described in the Supporting Information. The excerpted fig-

41 ures are reused under agreement between MIT and the publishers of the articles (<https://libraries.mit.edu/scholarly/publishing/using-published-figures/>), where the
42 copyright is owned by the publishers.
43

44 **Residuals vs. Literature-Reported Values**

45 Residual analysis can help sniff out systematic or correlated errors in the results presented
46 in Fig. 3A of the main text. We can define residuals between the literature-reported values
47 and the MAP values in several different ways. Here, we will consider two definitions of the
48 residuals, normalized either to the literature-reported Tafel slopes,

$$\text{Residual Normalized to Reported} = \frac{T_{\text{reported}} - T_{\text{MAP}}}{T_{\text{reported}}}; \quad (1)$$

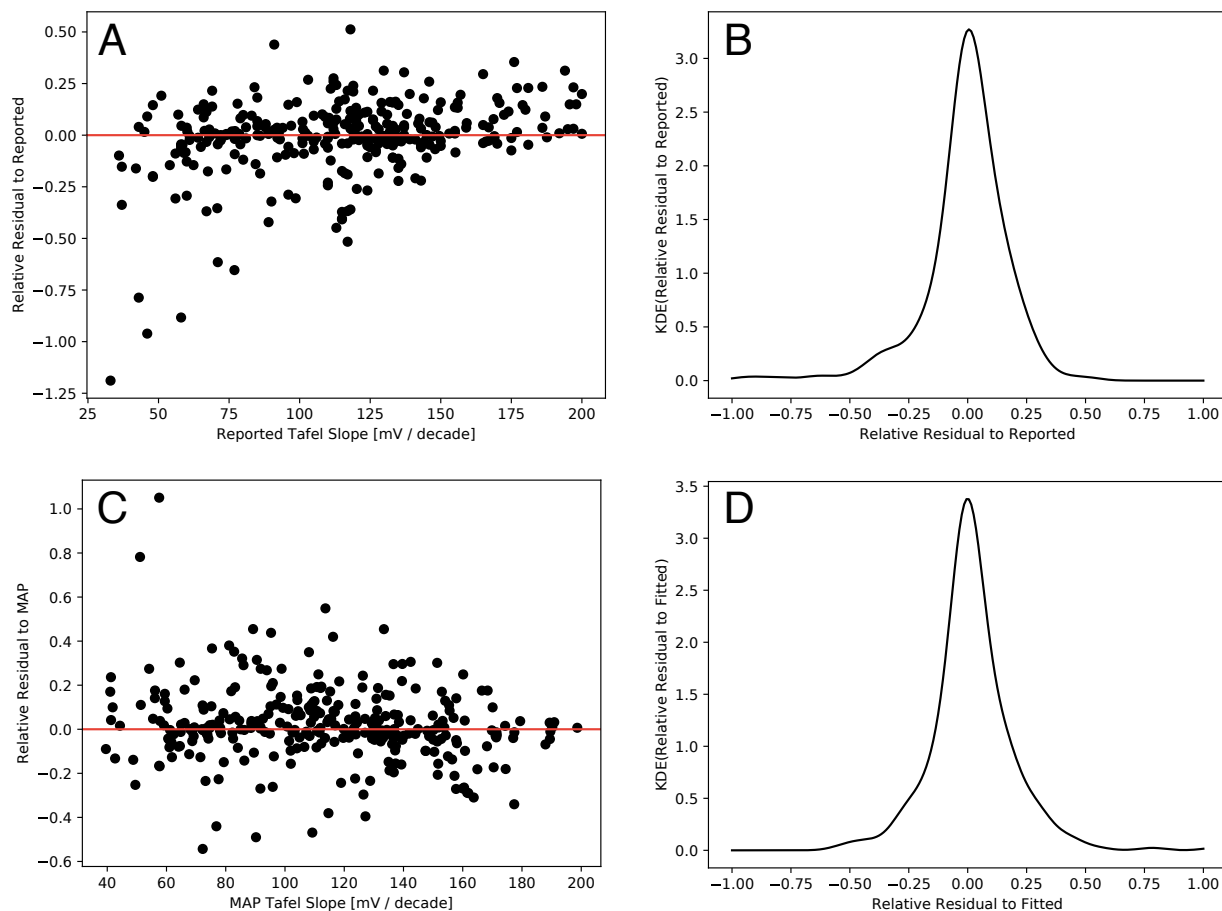
49 or to the MAP Tafel slopes,

$$\text{Residual Normalized to MAP} = \frac{T_{\text{reported}} - T_{\text{MAP}}}{T_{\text{MAP}}}; \quad (2)$$

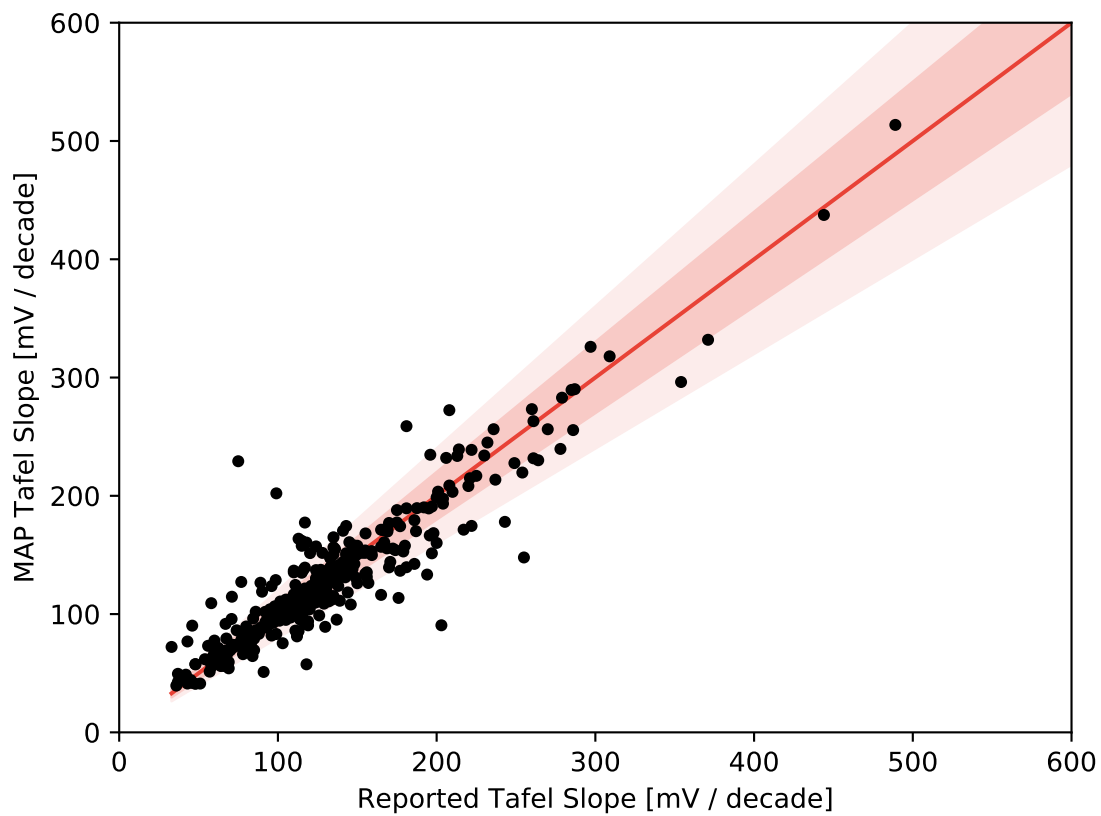
50 Figure 1 depicts plots of the residuals versus the literature-reported and MAP Tafel slopes (A
51 and C, respectively), as well as kernel density estimates of the distribution over the residuals
52 normalized to the literature-reported and MAP Tafel slopes (B and D, respectively). To the
53 eye, the residuals appear roughly unbiased around zero, and there appear to be no spurious
54 correlations between the residuals.

55 **Correlation Plot over Full Range**

56 Figure 2 depicts a correlation plot of the MAP Tafel slope versus the literature-reported
57 Tafel slope, including all datasets considered in this study.



Supplementary Figure 1: Residual Analysis. (A) Plot of the relative residual to the literature-reported Tafel slope, defined in Eq. (1), versus the literature-reported Tafel slope, including only reported Tafel slopes less than 200 mV/decade. (B) Kernel density estimate of the distribution over the relative residual to the literature-reported Tafel slope. (C) Plot of the relative residual to the MAP Tafel slope, defined in Eq. (1), versus the MAP Tafel slope, including only reported Tafel slopes less than 200 mV/decade. (D) Kernel density estimate of the distribution over the relative residual to the MAP Tafel slope.



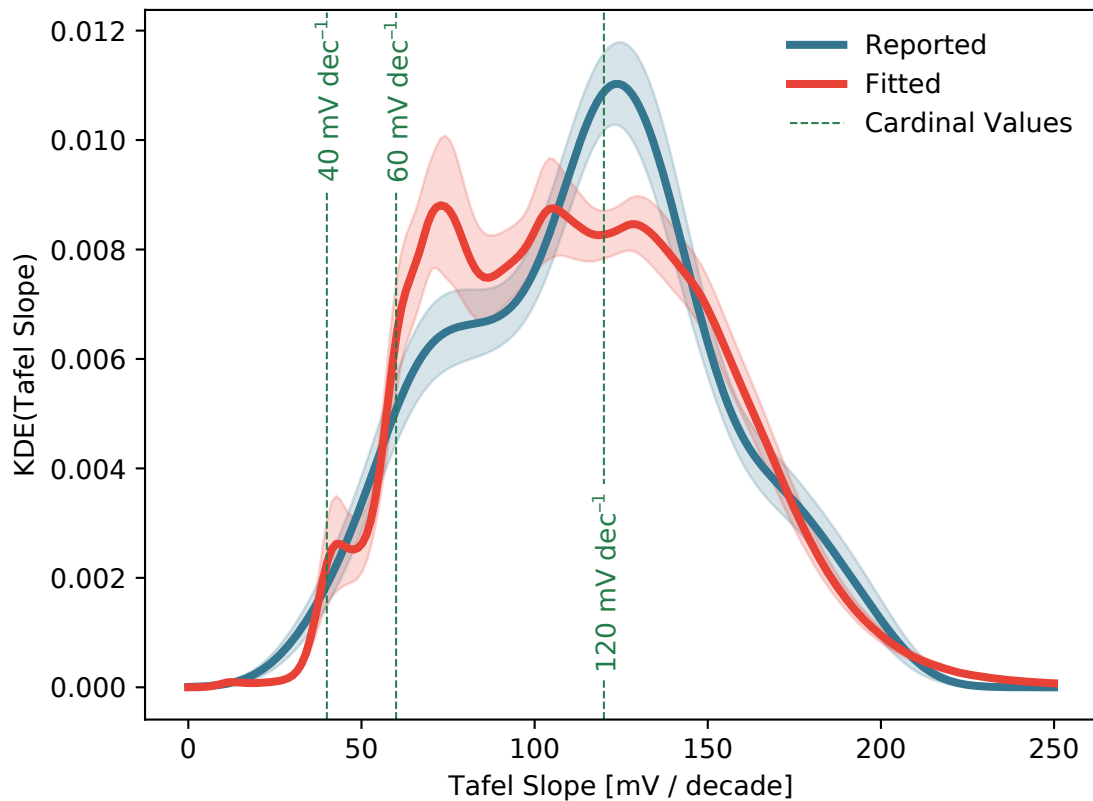
Supplementary Figure 2: Correlation plot of reported Tafel slopes from the literature against Tafel slopes fitted by our algorithm on identical data. The solid red line represents perfect agreement, while the red filled intervals are lines representing 10% and 20% relative error.

58 PDF Plot Using all Posterior Samples

59 For every single dataset considered in the study, we draw $N = 4 \times 10^4$ samples from the
60 posterior distribution over the Tafel slope. In Fig. 3C in the main text, we depict a kernel
61 density estimate of the distribution over the MAP Tafel slope from each of these posterior
62 distributions. We choose to display this data because the MAP Tafel slope is a straightfor-
63 ward point estimate of the Tafel slope given a posterior distribution over the parameter, and
64 hence is likely the quantity one would quote if asked what *the* Tafel slope of a catalyst is.
65 However, the averaging operation involved in computing the MAP Tafel slope can collapse
66 broad features in the posterior distribution down to a single value; this is especially true in
67 the case of bimodal posterior distributions arising from insufficient datasets. Figure 3 depicts
68 a kernel density estimate of the distribution over the Tafel slope using all samples collected
69 from the posterior distribution for each dataset. The essential conclusions reported in the
70 main text are upheld when examining the data in Fig. 3. A very small preference for Tafel
71 slopes around 45 mV/decade emerges in this analysis. However, given the small amount
72 of total distributional mass under this peak and the high degree of sampling variability (as
73 evinced by the bootstrap standard deviations), we do not believe it should be interpreted
74 strongly.

75 Catalyst Breakout Results

76 As described in the main text, we split out our results on the distributions over the Tafel
77 slope by catalyst material identity in order to confirm that our conclusion of a lack of Tafel
78 cardinality in CO₂ reduction catalysis is not an artifact of pooling together data from several
79 catalyst materials, each of which individually exhibit cardinality. Figures 4–9 depict these
80 results for catalysts containing Cu, Ag, Au, Sn, and Bi. Each figure has three panels: the
81 left-most panel plots a kernel density estimate of the distribution over Tafel slopes using
82 all samples from the posterior distribution, akin to Fig. 3. The center panel plots a kernel
83 density estimate of the distribution over the MAP Tafel slope from each dataset, akin to main



Supplementary Figure 3: Kernel density estimates (KDE) of the empirical probability distribution function of Tafel slopes reported in literature data (blue) and those refitted by our algorithm (red). Error intervals correspond to one standard deviation of bootstrapped resamples. Green dashed lines correspond to cardinal values of the Tafel slope.

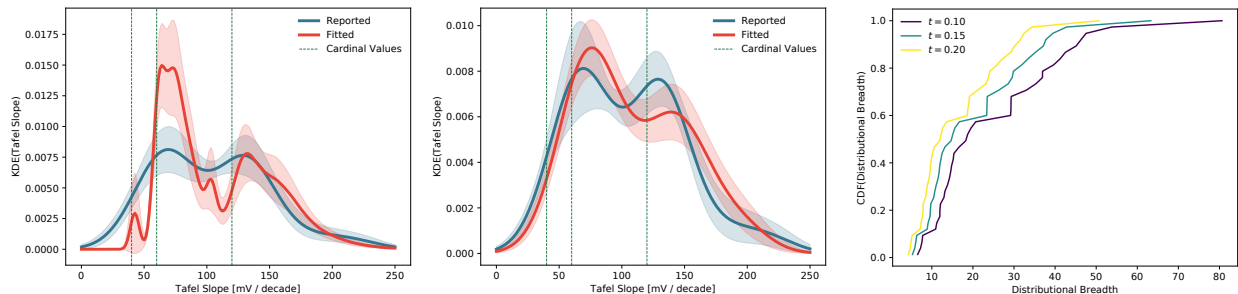
84 text Fig. 3C. The right-most panel plots a CDF of the distributional breadth B_i for each
85 dataset considered. The distributional breadth is parametrized by the threshold parameter
86 t , and is defined as,

$$B_i(t) = \text{CDF}_i^{-1}(1 - t) - \text{CDF}_i^{-1}(t); \quad (3)$$

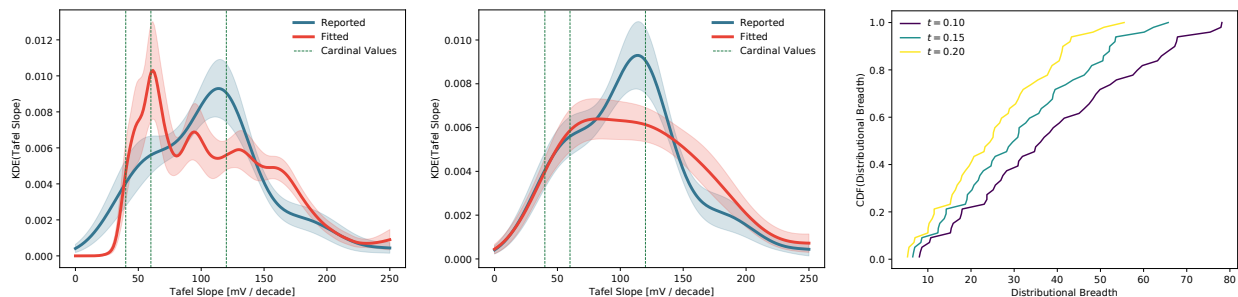
87 where $\text{CDF}_i(m_T)$ represents the CDF of the Tafel slope for the i 'th dataset. Intuitively,
88 a high distributional breadth implies that the experimental data measured in the dataset
89 does not provide information to pin down the value of the Tafel slope with high confidence.
90 Correspondingly, if the CDF of the distributional breadth increases quickly, then most of
91 the datasets in the catalyst material subset predict tight distributions over the Tafel slope.
92 Conversely, if the CDF of the distributional breadth climbs slowly, then several datasets in
93 the catalyst material subset do not determine a Tafel slope value with high confidence.

94 For some catalysts, the KDE constructed from all Tafel slope samples (left panel) and the
95 KDE constructed from the MAP Tafel slope samples (center panel) show different behavior.
96 The former plot looks more visually noisy than the latter plot; this is to be expected,
97 since taking the mean of the posterior distribution over the parameters is a "smoothing"
98 operation. The two ways of visualizing the data convey slightly distinct information, since the
99 KDE constructed from all samples preserves the uncertainty information retained in a single
100 fit, while the KDE constructed from the MAP Tafel slopes is the most direct comparison
101 to the distribution of literature values (which do not carry an associated uncertainty, in
102 most cases). In certain cases (Ag, Sn), the KDE comprising all samples appears to have
103 more defined peaks than the KDE comprising MAP samples. First, we note that in these
104 cases, the bootstrap standard errors for these peaks are much greater than in other areas
105 of the distribution, suggesting that this peaking behavior is controlled by a small number
106 of samples, and hence more variable with respect to a change in the specific datasets re-
107 analyzed in this study. Second, peaking behavior in the KDE comprising all samples that
108 does not appear in the KDE comprising MAP samples is a sign of some underlying data
109 insufficiency issues highlighted by Fig. 2 in the main text; these peaks can easily disappear

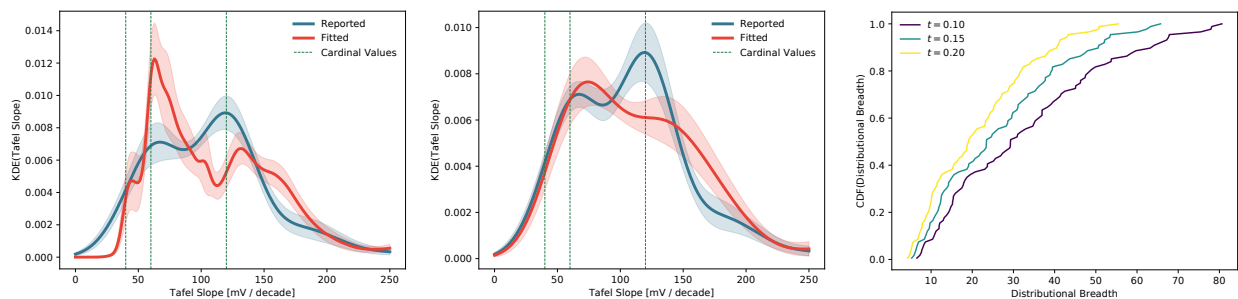
110 or be shifted upon measuring additional data. To declare confidently that a certain dataset
 111 espouses a cardinal Tafel slope preference, we contend that *both* ways of visualizing the
 112 distribution of Tafel slopes for a certain catalyst should show peaking around a cardinal value.
 113 This standard, while stringent, enforces that the available experimental data confidently
 114 determines a cardinal value of the Tafel slope, free of latent data insufficiency issues. While
 115 we observe this for the Bi breakout results in Fig. 9, the remainder of the catalyst breakout
 116 datasets do not meet this standard. Hence, though we do not foreclose the possibility
 117 that additional future data collection on these catalysts may reveal a cardinal Tafel slope
 118 preference, we argue that broadly, when considering the data extant in the literature, the
 119 typical CO₂ reduction catalyst does not exhibit a strong preference for cardinal values of the
 120 Tafel slope.



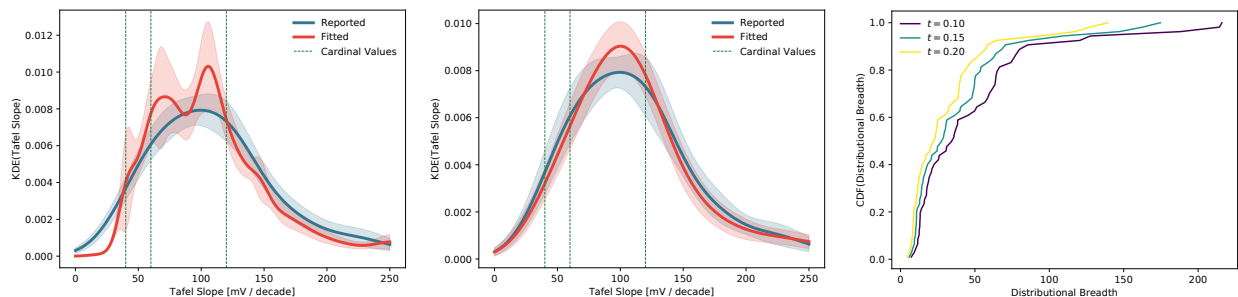
Supplementary Figure 4: Tafel Slope statistics for catalysts containing Ag ($N_{\text{datasets}} = 38$). (Left) Kernel density estimates (KDE) of the empirical probability distribution function of Tafel slopes reported in literature data (blue) and those refitted by our algorithm (red). Error intervals correspond to one standard deviation of bootstrapped resamples. Green dashed lines correspond to cardinal values of the Tafel slope. (Center) Same as (Left), but KDEs are computed using only the MAP Tafel Slope values for each dataset. (Right) CDF of the distributional breadth, as defined by Eq. (3).



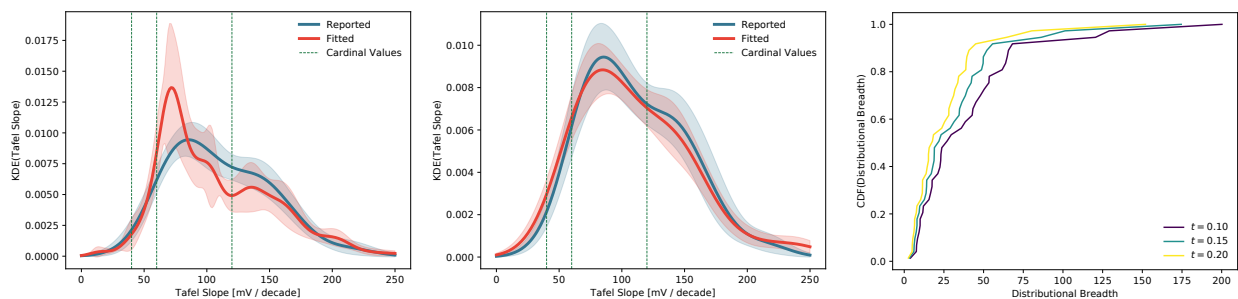
Supplementary Figure 5: Tafel Slope statistics for catalysts containing Au ($N_{\text{datasets}} = 50$). (Left) Kernel density estimates (KDE) of the empirical probability distribution function of Tafel slopes reported in literature data (blue) and those refitted by our algorithm (red). Error intervals correspond to one standard deviation of bootstrapped resamples. Green dashed lines correspond to cardinal values of the Tafel slope. (Center) Same as (Left), but KDEs are computed using only the MAP Tafel Slope values for each dataset. (Right) CDF of the distributional breadth, as defined by Eq. (3).



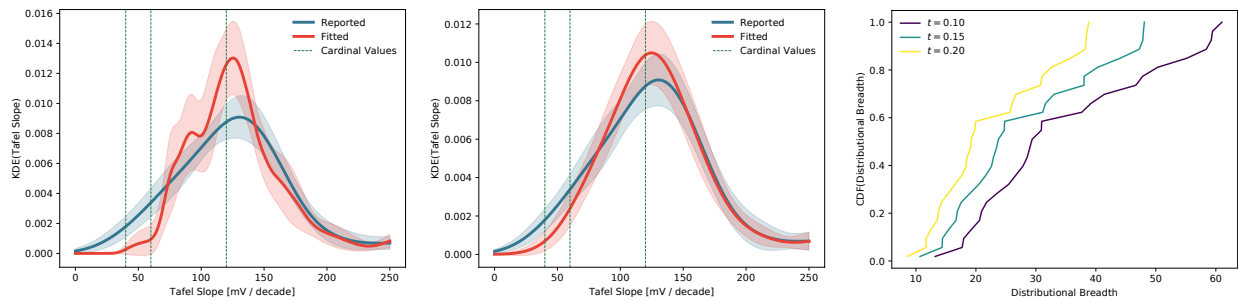
Supplementary Figure 6: Tafel Slope statistics for catalysts containing Ag or Au ($N_{\text{datasets}} = 88$). (Left) Kernel density estimates (KDE) of the empirical probability distribution function of Tafel slopes reported in literature data (blue) and those refitted by our algorithm (red). Error intervals correspond to one standard deviation of bootstrapped resamples. Green dashed lines correspond to cardinal values of the Tafel slope. (Center) Same as (Left), but KDEs are computed using only the MAP Tafel Slope values for each dataset. (Right) CDF of the distributional breadth, as defined by Eq. (3).



Supplementary Figure 7: Tafel Slope statistics for catalysts containing Cu ($N_{\text{datasets}} = 54$). (Left) Kernel density estimates (KDE) of the empirical probability distribution function of Tafel slopes reported in literature data (blue) and those refitted by our algorithm (red). Error intervals correspond to one standard deviation of bootstrapped resamples. Green dashed lines correspond to cardinal values of the Tafel slope. (Center) Same as (Left), but KDEs are computed using only the MAP Tafel Slope values for each dataset. (Right) CDF of the distributional breadth, as defined by Eq. (3).



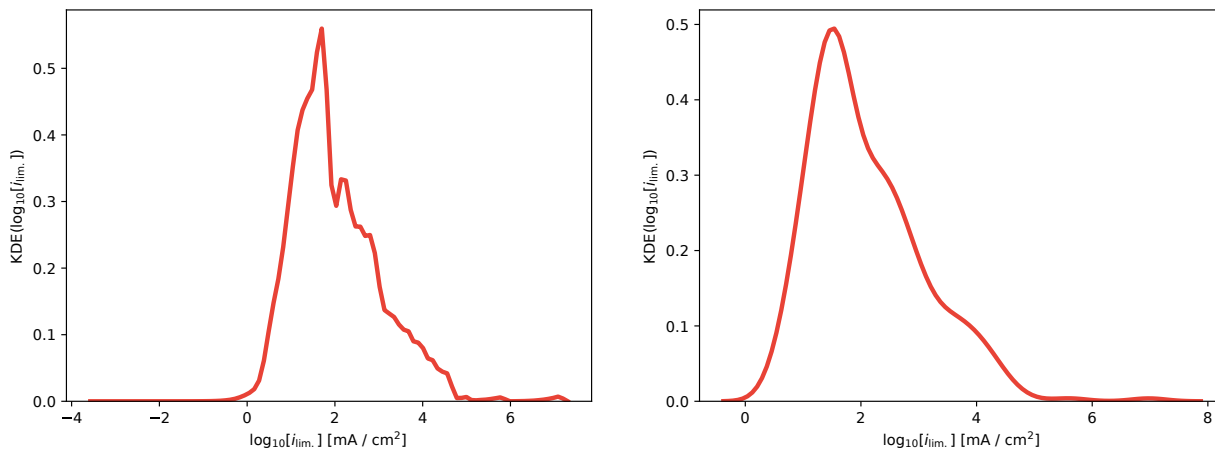
Supplementary Figure 8: Tafel Slope statistics for catalysts containing Sn ($N_{\text{datasets}} = 37$). (Left) Kernel density estimates (KDE) of the empirical probability distribution function of Tafel slopes reported in literature data (blue) and those refitted by our algorithm (red). Error intervals correspond to one standard deviation of bootstrapped resamples. Green dashed lines correspond to cardinal values of the Tafel slope. (Center) Same as (Left), but KDEs are computed using only the MAP Tafel Slope values for each dataset. (Right) CDF of the distributional breadth, as defined by Eq. (3).



Supplementary Figure 9: Tafel Slope statistics for catalysts containing Bi ($N_{\text{datasets}} = 27$). (Left) Kernel density estimates (KDE) of the empirical probability distribution function of Tafel slopes reported in literature data (blue) and those refitted by our algorithm (red). Error intervals correspond to one standard deviation of bootstrapped resamples. Green dashed lines correspond to cardinal values of the Tafel slope. (Center) Same as (Left), but KDEs are computed using only the MAP Tafel Slope values for each dataset. (Right) CDF of the distributional breadth, as defined by Eq. (3).

121 **Limiting Current Statistics**

122 Figure 10 depicts kernel density estimates of the distribution of fitted limiting currents i_{lim}
 123 from a re-analysis of literature data. Roughly, the distribution appears to be in agreement
 124 with the value of the transport-limited current density for CO₂ reduction at an aqueous
 flooded electrode.¹⁵⁰



Supplementary Figure 10: Limiting current statistics for all datasets analyzed in the study. (Left) Kernel density estimates (KDE) of the empirical probability distribution of the limiting current, i_{lim} fitted when interpreting the data through the model in main text Eq. (2). (Right) Same as (Left), but KDEs are computed using only the MAP limiting current values for each dataset.

125

126 **Bayesian Fitting**

127 **Mathematical Detail**

128 As quoted in the main text, Bayes' rule reads,

$$p(\mathbf{y} | \boldsymbol{\theta}) = \frac{p(\mathbf{y} | \boldsymbol{\theta}) \times p(\boldsymbol{\theta})}{p(\mathbf{y})} \tag{4}$$

129 In the context of this work, \mathbf{y} represents the measured current data at a set of voltage points.

130 We will use the subscript notation \mathbf{y}_k to denote a single current data point, where the index

131 $k = 1; \dots; N_{pts}$. The parameters of a model for interpreting current-voltage data are denoted

132 by $\mathcal{M}_k(\boldsymbol{\theta})$; in the context of this work, the relevant parameters for the limiting current model are
 133 i_{lim} , the limiting current density, i_0 , the exchange current density, and m_{T}^{-1} , the inverse Tafel
 134 slope. We will denote the model’s predictions at each voltage point by the subscript notation
 135 $\mathcal{M}_k(\boldsymbol{\theta})$.

136 To successfully apply Bayes’ rule to glean $\rho(\boldsymbol{\theta} | \mathbf{y})$, the posterior distribution over the
 137 model parameters given measured data, we need to identify mathematical forms for the
 138 prior distribution $\rho(\boldsymbol{\theta})$ and the likelihood function $\rho(\mathbf{y} | \boldsymbol{\theta})$. In all fits conducted in this study,
 139 we employ a uniform prior distribution (also known as an “uninformative” prior distribution)
 140 over a certain parameter range. Since the prior is uniform in the selected parameter range, as
 141 long as the range includes the values of the parameters for which $\rho(\boldsymbol{\theta} | \mathbf{y})$ has high probability
 142 mass, the choice of prior is unimportant (see further on for a numerical confirmation of this
 143 fact). Given this fact, the choice for the range of our uniform prior is determined by first
 144 using a standard nonlinear least-squares optimization algorithm (TRF) to determine a point
 145 estimate of the optimal set of parameters, $\boldsymbol{\theta}_{\text{opt}}$. Formally,

$$\begin{aligned}
 & \boldsymbol{\theta}_{\text{opt}} = \underset{\boldsymbol{\theta}}{\text{arg min}} \sum_{k=1}^{N_{\text{pts}}} [\mathbf{y}_k - \mathcal{M}_k(\boldsymbol{\theta})]^2 \quad (5)
 \end{aligned}$$

146 With the optimal parameters $\boldsymbol{\theta}_{\text{opt}}$ in hand, we select a uniform prior $\rho(\boldsymbol{\theta})$ that is supported in
 147 the range $[0; a \times \boldsymbol{\theta}_{\text{opt}}]$ for each parameter $i = 1 :::: N_{\text{params}}$. We choose the *very* conservative
 148 value $a = 10$ to ensure that the prior distribution has support over a very broad range
 149 around the optimal parameters. In principle, this choice of a results in a wide parameter
 150 space, which may affect the computational efficiency of a posterior sampling algorithm. In
 151 practice, we find very little computational disadvantage for choosing $a = 10$ as compared to
 152 $a = 2$ when using the No-U-Turn Sampler implemented in PyMC3.

153 The likelihood function for the data given the parameters, $\rho(\mathbf{y} | \boldsymbol{\theta})$, is determined by assum-
 154 ing that the experimental measurement represents a ground truth measurement described

155 by the model, polluted by unavoidable experimental error,

$$\mathbf{y}_k = \mathcal{M}_k(\boldsymbol{\theta}) + \boldsymbol{\epsilon}_k \quad (6)$$

156 We assume that errors at different data points are uncorrelated, and further assume that the
157 error $\boldsymbol{\epsilon}_i$ at any single data point is drawn from a Gaussian distribution with zero mean and
158 variance σ^2 ,

$$p(\boldsymbol{\epsilon}_k) = \frac{1}{\sqrt{2\pi}\sigma} \exp\left[-\frac{\boldsymbol{\epsilon}_k^2}{2\sigma^2}\right] \quad (7)$$

159 Because the errors at each point are uncorrelated, the likelihood now factorizes over all the
160 data points,

$$p(\mathbf{y}|\boldsymbol{\theta}) = \prod_{k=1}^{N_{\text{pts}}} \frac{1}{\sqrt{2\pi}\sigma} \exp\left[-\frac{(\mathbf{y}_k - \mathcal{M}_k(\boldsymbol{\theta}))^2}{2\sigma^2}\right] \quad (8)$$

161 With a likelihood function $p(\mathbf{y}|\boldsymbol{\theta})$ and a prior distribution $p(\boldsymbol{\theta})$ in hand, we can plug this
162 information into a Monte Carlo sampler of our choice to draw samples from the posterior
163 distribution $p(\boldsymbol{\theta}|\mathbf{y})$. Equation (8) also makes apparent how one can generalize the Bayesian
164 posterior sampling approach to more general models $\mathcal{M}(\boldsymbol{\theta})$. After we write down a suitable
165 model, we simply evaluate the model predictions with different parameters whenever we
166 need to compute the likelihood function for a given set of parameters during the sampling
167 procedure.

168 Gaussian Error Estimates from Nonlinear Optimization

169 The Bayesian posterior sampling approach advanced in this work provides a way to glean
170 distributional uncertainty information about the estimated values of model parameters given
171 observed data. A similar set of information can also be obtained by analyzing the Hessian
172 matrix determined by a nonlinear optimization algorithm seeking an optimal point estimate

173 of the model parameters. Specifically, if the optimizer seeks to minimize a loss function,

$$\mathcal{L}(\boldsymbol{\theta}) = \frac{1}{2} \sum_{k=1}^{N_{\text{pts}}} [\mathbf{y}_k - \mathcal{M}_k(\boldsymbol{\theta})]^2 ; \quad (9)$$

174 then it often also produces an estimate of the Hessian,

$$\mathbf{H}_{ij} = \frac{\partial^2 \mathcal{L}}{\partial \theta_i \partial \theta_j} ; \quad (10)$$

175 evaluated at the optimal value of the parameters $\boldsymbol{\theta}^*$. If we assume that the experimental
 176 data is generated by the random process described by Eq. (6), and further assume that the
 177 errors at different data points are uncorrelated and drawn from Gaussian distributions with
 178 mean zero and variance σ^2 , then we can form a Gaussian approximation to the posterior
 179 distribution around $\boldsymbol{\theta}^*$,

$$\rho(\boldsymbol{\theta} | \mathbf{y}) \approx \frac{1}{(2\pi)^{d/2} (\det \mathbf{H})^{1/2}} \exp \left[-\frac{1}{2} (\boldsymbol{\theta} - \boldsymbol{\theta}^*)^T \mathbf{H} (\boldsymbol{\theta} - \boldsymbol{\theta}^*) \right] ; \quad (11)$$

180 where d is the number of parameters being estimated, and \mathbf{H} is guaranteed to be positive
 181 definite by virtue of being evaluated at the optimal point $\boldsymbol{\theta}^*$.

182 We stress that the expression provided by Eq. (11) is an *approximation* to the true pos-
 183 terior distribution; due to its Gaussian form, this expression can never accurately represent
 184 bimodality in the posterior distribution. In this sense, the Bayesian sampling approach is
 185 superior, although it comes at significant additional computational expense as d increases.
 186 In this work, $d = 3$, and this additional expense is essentially negligible given the compu-
 187 tational power available on a typical laptop or desktop computer. Hence, we suggest that
 188 posterior distributions over the Tafel slope fitted using the model in Eq. (2) of the main
 189 text should always be computed using the Bayesian posterior sampling algorithm described
 190 in the previous section. We have simply included mention of the Gaussian approximation
 191 for the sake of completeness, and to guide possible future work that attempts to fit models

192 with significantly more parameters.

193 Sensitivity to Error Distribution Width

194 One important parameter of the Bayesian fitting approach is the width of the normal distri-
195 bution governing the probability of deviations from the model, which arises when evaluating
196 the quantity $p(y_j)$ in Bayes' rule. Figure 11 studies the sensitivity of the posterior dis-
197 tribution over the Tafel slope to the parameter σ , the standard deviation of the normal
distribution governing the statistics of the model error. As expected, lowering the value of

Supplementary Figure 11: Sensitivity to the width of the error distribution at each point for a simple fit to synthetic data. (A) Synthetic data sampled from a model with an underlying Tafel slope of 80 mV/decade. (B) Several traces of the posterior distribution computed using different values of σ , the standard deviation of the normal error distribution at each point.

198

199 σ causes the algorithm to become more confident in its estimate. At $\sigma = 0.01$ logarithmic
200 units, the model essentially nails the true Tafel slope of 80 mV/decade. For larger values of σ
201 a clear distributional drift to lower values of the Tafel slope is observed. This occurs because
202 most of the data in Fig. 11A lies in the plateau region, and the model faces less penalty for
203 down-weighting these points as the value of σ is increasing. Hence, the model drifts to larger
204 slopes on the Fig. 11A plot, which corresponds to lower values of the Tafel slope. Note that
205 the distributional widening is significantly greater than the drift in the mean, suggesting
206 that we should not put much stock into the mean drift. The upshot: for high values of the

207 parameter, this particular set of data does not contain enough information to pin down
208 the value of the Tafel slope accurately.

209 Sensitivity to Prior Distribution

210 As explained in the main text, our Bayesian approach requires specification of a prior dis-
211 tribution $p(\theta)$ over the parameters. Since we know very little about the true distribution of
212 the Tafel slope at the outset, we choose an uninformative uniform box prior over the interval
213 $[0; a_i]$ for each parameter θ_i , where a_i is the optimal value of the parameter gleaned from
214 the TRF algorithm described in the Methods section. Here, we conduct a sensitivity analysis
215 on the a_i parameter. Given that we are using an uninformative prior, we should expect that
216 the prior width should not influence the posterior distribution as long as the data expresses
217 some opinion about the ideal value of the parameters. Figure 12 depicts the results of the
sensitivity analysis on a set of synthetic data. Indeed, as expected, the posterior distribu-

Supplementary Figure 12: Sensitivity to the width of the uniform prior distribution bounds.
(A) Synthetic data sampled from a model with an underlying Tafel slope of 80 mV/decade.
(B) Several traces of the posterior distribution computed using different values of a_i , a pa-
rameter influencing the width of the prior distribution fed to the Bayesian posterior sampling
algorithm. All posterior distributions are computed with $\sigma = 0.05$.

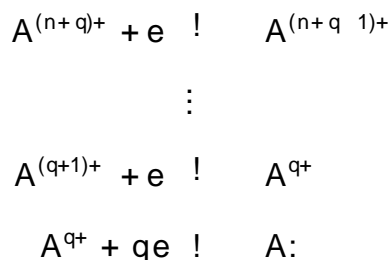
218

219 tions are insensitive to the choice of prior. Note that in all fits considered in the main text,
220 we use a value of $a_i = 10$, as mentioned in the Methods section.

221 Derivations

222 Cardinal Tafel Slopes Equation

We will work with a generic reaction scheme, assuming that we begin with a starting species $A^{(n+q)+}$ which undergoes n electron transfers prior to the rate-determining step, and then q electron transfers at the RDS. In practice n will be an integer, and q will be either zero or one. Here we assume the reaction taking place is reductive; however, the derivation is entirely analogous for an equivalent oxidation reaction. Schematically, the reactions read,



223 The overall current is determined by the rate of the RDS. Assuming Butler-Volmer kinetics
 224 for the forward rate constant of the RDS, we have,

$$\text{rate} = k_0 f a_{A^{q+}} \exp\left[-\frac{q\alpha e}{k_B T} (\phi - \phi_{eq})\right] a_A \exp\left[\frac{q(1-\alpha) e}{k_B T} (\phi - \phi_{eq})\right] g; \quad (12)$$

225 where k_0 is the rate prefactor (sometimes called the Arrhenius prefactor), a_i is the activity
 226 of species i , $(k_B T)^{-1}$ is the inverse thermodynamic temperature, e is the fundamental
 227 charge, α is the symmetry coefficient, ϕ is the applied potential, and ϕ_{eq} is the equilibrium
 228 potential for the RDS. At sufficiently high reductive overpotentials $\phi - \phi_{eq} \ll 0$, only the
 229 first term survives,

$$\text{rate} = k_0 a_{A^{q+}} \exp\left[-\frac{q\alpha e}{k_B T} (\phi - \phi_{eq})\right]; \quad (13)$$

230 To make further progress, we have to solve for the activity of the intermediate species A^{q+}
 231 in terms of the activity of the reactant species for the overall reaction, $A^{(n+q)+}$. If we assume

232 that all steps prior to the RDS are fast and equilibrated, we can extract this activity
 233 by analyzing the thermodynamics of the steps prior to the RDS. The free energy change
 234 associated with the r th reaction reads,

$$F_r = -RT \ln a_{A^{(n+q-r)+}} + RT \ln a_{A^{(n+q-(r+1))+}} + e : \quad (14)$$

Then, the equilibrium constant for reaction r goes as,

$$K_r = \exp\left[-\frac{F_r}{RT}\right] \quad (15)$$

$$K_r = \frac{a_{A^{(n+q-(r+1))+}}}{a_{A^{(n+q-r)+}}} \exp\left[-\frac{e}{RT}\right] \quad (16)$$

$$K_r = \mathcal{K}_r \exp\left[-\frac{e}{RT}\right]; \quad (17)$$

where \mathcal{K}_r is defined by Eq. (17), and is independent of potential. Since Eq. (17) holds for all reactions r before the RDS, we can easily solve for the activity of the intermediate,

$$a_{A^{q+}} = \prod_{r=1}^{\#} \mathcal{K}_r \exp\left[-\frac{ne}{RT}\right] a_{A^{(n+q)+}} \quad (18)$$

$$a_{A^{q+}} = \prod_{r=1}^{\#} \mathcal{K}_r \exp\left[-\frac{ne}{RT} \left(\frac{e_{eq}}{e}\right)\right] \exp\left[-\frac{ne}{RT} \left(\frac{e_{eq}}{e}\right)\right] a_{A^{(n+q)+}} : \quad (19)$$

Plugging back into Eq. (13),

$$\text{rate} = k_0 \prod_{r=1}^{\#} \mathcal{K}_r \exp\left[-\frac{ne}{RT} \left(\frac{e_{eq}}{e}\right)\right] \exp\left[-\frac{ne}{RT} \left(\frac{e_{eq}}{e}\right)\right] a_{A^{(n+q)+}} \exp\left[-\frac{qe(1-\alpha)}{RT} \left(\frac{e_{eq}}{e}\right)\right] \quad (20)$$

$$\text{rate} = k_0 \prod_{r=1}^{\#} \mathcal{K}_r \exp\left[-\frac{ne}{RT} \left(\frac{e_{eq}}{e}\right)\right] a_{A^{(n+q)+}} \exp\left[-\frac{e}{RT} \left(\frac{e_{eq}}{e}\right) (n+q(1-\alpha))\right] : \quad (21)$$

235 This is a mess, but we only care about the potential-dependent terms when extracting the
 236 Tafel slope, which means we only have to consider the last factor on the RHS. Taking the

237 logarithm yields,

$$\log [\text{rate}] = \frac{e}{k_B T} (\eta_{\text{eq}}) (n + q (1 - \theta)) + C; \quad (22)$$

238 where C is a constant independent of potential. For a reduction reaction, the Tafel slope is
 239 defined as,

$$\text{Tafel Slope} = \frac{\partial \log_{10} [\text{rate}]}{\partial \left(\frac{e}{k_B T} \eta_{\text{eq}} \right)}^{-1}; \quad (23)$$

240 Hence, we have,

$$\text{Tafel Slope} = \left[\log_{10} (\exp(1)) \frac{e}{k_B T} \right]^{-1} \frac{1}{n + q (1 - \theta)}; \quad (24)$$

241 Appropriate unit scalings yield,

$$\text{Tafel Slope} = \frac{60 \text{ mV/decade}}{n + q (1 - \theta)}; \quad (25)$$

242 which reduces to the equation quoted in the main text when $\theta = 1 = 2$.

243 Physical Non-Idealities

244 Tafel Slopes with Physical Non-Idealities

245 Eq. (25) already accounts for the non-ideality effects introduced by $\theta = 1 = 2$. If we assume
 246 that the CO_2 adsorption step has partial charge transfer character quantified by θ , then
 247 despite the fact that the adsorption step is purely chemical, we assume that its equilibrium
 248 constant carries a non-integer order dependence on the applied potential. This can also be
 249 motivated by considering the formation of a permanent dipole on the surface species, which
 250 can access additional thermodynamic stabilization due to a dipole Stark shift from electric
 251 fields present at the interface. The manner in which surface dipole formation augments the
 252 Tafel slope depends on whether or not the CO_2 adsorption step is the rate determining
 253 step. For the case $\theta; q = (0; 1)$, the adsorption step is the RDS. The Frumkin correction

254 attenuates the applied potential for the rate-determining step by a factor f , which simply
 255 multiplies the latter term in the denominator of Eq. (25). Hence, the Tafel slope for $(\eta; q) =$
 256 $(0; 1)$ is,

$$\text{Tafel Slope} = \frac{60 \text{ mV/decade}}{f(1 - \eta)}; \quad (26)$$

257 For the case $(\eta; q) = (1; 0)$, the adsorption step is the RDS, and rather than contributing
 258 $n = 1$ to the order, it instead contributes according to the η parameter,

$$\text{Tafel Slope} = \frac{60 \text{ mV/decade}}{\eta}; \quad (27)$$

259 Finally, for the case $(\eta; q) = (1; 1)$, the adsorption step occurs before the RDS, and the Tafel
 260 slope reads,

$$\text{Tafel Slope} = \frac{60 \text{ mV/decade}}{1 + f(1 - \eta)}; \quad (28)$$

261 Sensitivities to Parameter Bounds

262 Figures 13 and 14 study the sensitivity of the distributional results presented in Fig. 4
 263 of the main text to the bounds of the uniform distributions over non-ideality parameters.
 264 Broadly, our claim is supported by the sensitivity analysis; within reasonable parameter
 265 bounds, we still see that we can get essentially arbitrary distributional shapes depending on
 266 the nonidealities included in the model.

267 Multiple Kinetic Regimes

268 Here, we examine the consequences of fitting current-voltage data from a system exhibiting
 269 multiple kinetic regimes to a model that only allows a single Tafel slope (as in Eq. (2) in the
 270 main text) by analyzing synthetic data. The synthetic data is generated from the model,

$$\frac{1}{i(E)} = \frac{1}{i_{\text{lim}}} + \frac{1 + \exp\left[-\frac{e[k_B T]}{1 - \eta_1} \frac{[E - E_{\text{eq},1}]}{[E - E_{\text{eq},2}]} \right]}{\exp\left[-\frac{e[k_B T]}{1 - \eta_1} \frac{[E - E_{\text{eq},1}]}{[E - E_{\text{eq},2}]} \right]}; \quad (29)$$

Supplementary Figure 13: Several synthetic kernel density estimates of the probability distributions over the Tafel slope generated from including random values of different parameters governing physical non-idealities. Different panels use different uniform distributions over the symmetry coefficient parameter, β .

Supplementary Figure 14: Several synthetic kernel density estimates of the probability distributions over the Tafel slope generated from including random values of different parameters governing physical non-idealities. Different panels use different uniform distributions over the Frumkin correction parameter, f .

271 where E is the applied potential, and the model has free fitting parameters, i_{lim} , $E_{eq,1}$,
 272 and $E_{eq,2}$. This model can be shown to arise when a reaction proceeds through a rate-
 273 limiting surface reaction involving a surface intermediate generated through a one-electron
 274 transfer, and present at non-negligible surface coverages. The specifics of how this model
 275 arises are less relevant to this analysis than the fact that the model exhibits two different
 276 Tafel regimes. When $\alpha = 1/2$, the first regime has Tafel slope $m_T = 40 \text{ mV decade}^{-1}$ for
 277 $E_{eq,1} < E < E_{eq,2}$, and the second regime has a Tafel slope $m_T = 120 \text{ mV decade}^{-1}$ for
 278 $E > E_{eq,2}$, before topping out at the limiting current i_{lim} .

Supplementary Figure 15: (A) Current-voltage trace generated from Eq. (29) using the
 parameters $\alpha = 1/2$, $i_{lim} = 100 \text{ mA cm}^{-2}$, $E_{eq,1} = 0.05 \text{ V}$, and $E_{eq,2} = 0.15 \text{ V}$ (red trace),
 along with artificially noised data sampled from the model (black points). (B) Current-
 voltage traces evaluated from the MAP fit parameters for Eq. (2) in the main text and Eq.
 (29), along with the noised data used for the fits (black points). (C) Posterior distribution
 over the Tafel slope for the model described by Eq. (2) in the main text.

279 Figure 15A shows a trace of the current-voltage behavior predicted by Eq. (29), with
 280 parameters $\alpha = 1/2$, $i_{lim} = 100 \text{ mA cm}^{-2}$, $E_{eq,1} = 0.05 \text{ V}$, and $E_{eq,2} = 0.15 \text{ V}$, as well
 281 as artificially noised data sampled from this model at a sparsely sampled set of voltage
 282 points. Figure 15B shows current-voltage traces from both Eq. (29) (red) and Eq. (2)
 283 from the main text (blue), each evaluated under the MAP parameters determined from their
 284 respective Bayesian fits. Finally, Fig. 15C shows the Bayes posterior distribution for the
 285 Tafel slope fitted using Eq. (2) from the main text. As expected, when using the single
 286 Tafel regime model to fit data generated from multiple Tafel regimes, the MAP value of the
 287 Tafel slope does not coincide with the Tafel slope from either kinetic regime in Eq. (29).

Supplementary Figure 16: Posterior distributions for β , i_{lim} , $E_{eq;1}$, and $E_{eq;2}$ (A, B, C, D, respectively) gleaned from Bayesian posterior sampling on the artificially noised data in Fig. 15A.

288 However, as illustrated in Fig. 16, when the original data is fit to Eq. (29), the posterior
289 distributions are peaked around the true values of the parameters.

290 This analysis yields two important takeaways. First, it lends credence to the idea that
291 fitting a single Tafel slope to data collected under multiple Tafel regimes, each individu-
292 ally exhibiting a cardinal Tafel slope, can produce an n -cardinal value of the Tafel slope,
293 providing an alternative possible explanation for the lack of observed cardinality in the lit-
294 erature analysis in the main text. Second, and perhaps more importantly, it shows that
295 the Bayesian framework presented here can successfully estimate the parameters of more
296 complicated physical models that incorporate the effects of multiple different Tafel regimes,
297 or some of the physical nonidealities discussed in the main text. Practically, we furnish the
298 following recommendation: if one knows in advance that multiple kinetic regimes are at play
299 in a set of current-voltage data, and the nature of these regimes can be encoded into a ki-
300 netic model like Eq. (29), then one should carry out Bayesian fitting to such a model. In the
301 absence of sufficient independent evidence to pin down a kinetic model that resolves multiple
302 kinetic regimes, Eq. (2) from the main text is a viable alternative, but one should be very
303 cautious about over-interpreting the mechanistic implications of a Tafel slope determined in
304 this manner.

References

- (1) Manthiram, K.; Beberwyck, B. J.; Alivisatos, A. P. Enhanced Electrochemical Methanation of Carbon Dioxide with a Dispersible Nanoscale Copper Catalyst. *J. Am. Chem. Soc.* 136 13319{13325, DOI:10.1021/ja5065284 , (2014).
- (2) Chen, Y.; Li, C. W.; Kanan, M. W. Aqueous CO₂ Reduction at Very Low Overpotential on Oxide-Derived Au Nanoparticles. *J. Am. Chem. Soc.* 134 19969{19972, DOI: 10.1021/ja309317u , (2012).
- (3) Noda, H.; Ikeda, S.; Yamamoto, A.; Einaga, H.; Ito, K. Kinetics of Electrochemical Reduction of Carbon Dioxide on a Gold Electrode in Phosphate Buffer Solution. *Bull. Chem. Soc. Jpn.* 68 1889{1895, DOI:10.1246/bcsj.68.1889 , (1995).
- (4) Ma, M.; Trześniewski, B. J.; Xie, J.; Smith, W. A. Selective and Efficient Reduction of Carbon Dioxide to Carbon Monoxide on Oxide-Derived Nanostructured Silver Electrocatalysts. *Angew. Chem. Int. Ed.* 55 9748{9752, DOI:10.1002/anie.201604654 , (2016).
- (5) Wu, J.; Yadav, R. M.; Liu, M.; Sharma, P. P.; Tiwary, C. S.; Ma, L.; Zou, X.; Zhou, X.-D.; Yakobson, B. I.; Lou, J.; Ajayan, P. M. Achieving Highly Efficient, Selective, and Stable CO₂ Reduction on Nitrogen-Doped Carbon Nanotubes. *ACS Nano* 9 5364{5371, DOI: 10.1021/acsnano.5b01079, (2015).
- (6) Gu, J.; Heroguez, F.; Luterbacher, J.; Hu, X. Densely Packed, Ultra Small SnO Nanoparticles for Enhanced Activity and Selectivity in Electrochemical CO₂ Reduction. *Angew. Chem. Int. Ed.* 57 2943{2947, DOI:10.1002/anie.201713003 , (2018).
- (7) Li, X.; Bi, W.; Chen, M.; Sun, Y.; Ju, H.; Yan, W.; Zhu, J.; Wu, X.; Chu, W.; Wu, C.; Xie, Y. Exclusive Ni(111) Sites Realize Near-Unity CO Selectivity for Electrochemical CO₂ Reduction. *J. Am. Chem. Soc.* 139 14889{14892, DOI:10.1021/jacs.7b09074 , (2017).

- 330 (8) Zhu, M.; Chen, J.; Huang, L.; Ye, R.; Xu, J.; Han, Y. Covalently Grafting Cobalt
331 Porphyrin onto Carbon Nanotubes for Efficient CO₂ Electroreduction. *Angew. Chem.*
332 *Int. Ed.* 58, 6595{6599, DOI:10.1002/anie.201900499 , (2019).
- 333 (9) Wang, Y.; Liu, J.; Wang, Y.; Al-Enizi, A. M.; Zheng, G. Tuning of CO
334 ₂ Reduction Selectivity on Metal Electrocatalysts. *Small* 13, 1701809, DOI:
335 10.1002/smll.201701809 , (2017).
- 336 (10) Ma, T.; Fan, Q.; Tao, H.; Han, Z.; Jia, M.; Gao, Y.; Ma, W.; Sun, Z. Het-
337 erogeneous electrochemical CO₂ reduction using nonmetallic carbon-based cat-
338 alysts: current status and future challenges *Nanotechnology* 28 472001, DOI:
339 10.1088/1361-6528/aa8f6f , (2017).
- 340 (11) Liu, Y.; Chen, S.; Quan, X.; Yu, H. Efficient Electrochemical Reduction of Carbon
341 Dioxide to Acetate on Nitrogen-Doped Nanodiamond *J. Am. Chem. Soc.* 137 11631{
342 11636, DOI:10.1021/jacs.5b02975 , (2015).
- 343 (12) Su, P.; Iwase, K.; Nakanishi, S.; Hashimoto, K.; Kamiya, K. Nickel-Nitrogen-Modi ed
344 Graphene: An Efficient Electrocatalyst for the Reduction of Carbon Dioxide to Carbon
345 Monoxide. *Small* 12, 6083{6089, DOI:10.1002/smll.201602158 , (2016).
- 346 (13) Shao, P.; Ci, S.; Yi, L.; Cai, P.; Huang, P.; Cao, C.; Wen, Z. Hollow CuS Microcube
347 Electrocatalysts for CO₂ Reduction Reaction. *ChemElectroChem* 4 2593{2598, DOI:
348 10.1002/celec.201700517 , (2017).
- 349 (14) Xu, J.; Kan, Y.; Huang, R.; Zhang, B.; Wang, B.; Wu, K.-H.; Lin, Y.; Sun, X.; Li, Q.;
350 Centi, G.; Su, D. Revealing the Origin of Activity in Nitrogen-Doped Nanocarbons
351 towards Electrocatalytic Reduction of Carbon Dioxide. *ChemSusChem* , 91085{1089,
352 DOI: 10.1002/cssc.201600202 , (2016).
- 353 (15) Medina-Ramos, J.; DiMeglio, J. L.; Rosenthal, J. Efficient Reduction of CO₂ to CO

- 354 with High Current Density Using in Situ or ex Situ Prepared Bi-Based MaterialsJ.
355 Am. Chem. Soc. 1368361{8367, DOI:10.1021/ja501923g , (2014).
- 356 (16) Ma, M.; Liu, K.; Shen, J.; Kas, R.; Smith, W. A. In Situ Fabrication and Reactivation
357 of Highly Selective and Stable Ag Catalysts for Electrochemical CO Conversion.
358 ACS Energy Lett. 3 1301{1306, DOI:10.1021/acsenergylett.8b00472 , (2018).
- 359 (17) Zhang, S.; Kang, P.; Meyer, T. J. Nanostructured Tin Catalysts for Selective Electro-
360 chemical Reduction of Carbon Dioxide to FormateJ. Am. Chem. Soc. 1361734{1737,
361 DOI: 10.1021/ja4113885 , (2014).
- 362 (18) Jiang, X.; Cai, F.; Gao, D.; Dong, J.; Miao, S.; Wang, G.; Bao, X. Electrocatalytic re-
363 duction of carbon dioxide over reduced nanoporous zinc oxideElectrochem. Commun.
364 68, 67{70, DOI: 10.1016/j.elecom.2016.05.003 , (2016).
- 365 (19) Chen, Y.; Kanan, M. W. Tin Oxide Dependence of the CO₂ Reduction Efficiency
366 on Tin Electrodes and Enhanced Activity for Tin/Tin Oxide Thin-Film Catalysts. J.
367 Am. Chem. Soc. 1341986{1989, DOI:10.1021/ja2108799 , (2012).
- 368 (20) Chang, Z.; Huo, S.; Zhang, W.; Fang, J.; Wang, H. The Tunable and Highly Se-
369 lective Reduction Products on Ag@Cu Bimetallic Catalysts Toward CO₂ Elec-
370 trochemical Reduction Reaction. J. Phys. Chem. C 121 11368{11379, DOI:
371 10.1021/acs.jpcc.7b01586 , (2017).
- 372 (21) Koh, J. H.; Won, D. H.; Eom, T.; Kim, N.-K.; Jung, K. D.; Kim, H.; Hwang, Y. J.;
373 Min, B. K. Facile CO₂ Electro-Reduction to Formate via Oxygen Bidentate Intermedi-
374 ate Stabilized by High-Index Planes of Bi Dendrite CatalystACS Catal. 7, 5071{5077,
375 DOI: 10.1021/acscatal.7b00707 , (2017).
- 376 (22) Jianping, Q.; Juntao, T.; Jie, S.; Cuiwei, W.; Mengqian, Q.; Zhiqiao, H.; Jianmeng, C.;
377 Song, S. Preparation of a silver electrode with a three-dimensional surface and its

- 378 performance in the electrochemical reduction of carbon dioxide. *Electrochim. Acta*
379 203, 99{108, DOI: 10.1016/j.electacta.2016.03.182 , (2016).
- 380 (23) Qiu, Y.; Du, J.; Dong, W.; Dai, C.; Tao, C. Selective conversion of CO₂ to for-
381 mate on a size tunable nano-Bi electrocatalyst. *J. CO₂ Util.* 20, 328{335, DOI:
382 10.1016/j.jcou.2017.05.024 , (2017).
- 383 (24) Karapinar, D.; Zitolo, A.; Huan, T. N.; Zanna, S.; Taverna, D.; Galvao Tizei, L. H.;
384 Giaume, D.; Marcus, P.; Mougel, V.; Fontecave, M. Carbon-Nanotube-Supported Cop-
385 per Polyphthalocyanine for Efficient and Selective Electrocatalytic CO₂ Reduction to
386 CO. *ChemSusChem* 13, 173{179, DOI: 10.1002/cssc.201902859 , (2020).
- 387 (25) Luan, C.; Shao, Y.; Lu, Q.; Gao, S.; Huang, K.; Wu, H.; Yao, K. High-
388 Performance Carbon Dioxide Electrocatalytic Reduction by Easily Fabricated Large-
389 Scale Silver Nanowire Arrays. *ACS Appl. Mater. Interfaces* 10, 17950{17956, DOI:
390 10.1021/acsami.8b03461 , (2018).
- 391 (26) Peng, Y.; Wu, T.; Sun, L.; Nsanzimana, J. M. V.; Fisher, A. C.; Wang, X. Selec-
392 tive Electrochemical Reduction of CO₂ to Ethylene on Nanopores-Modified Copper
393 Electrodes in Aqueous Solution. *ACS Appl. Mater. Interfaces* 9, 32782{32789, DOI:
394 10.1021/acsami.7b10421 , (2017).
- 395 (27) Lu, H.; Zhang, L.; Zhong, J. H.; Yang, H. G. Partially Oxidized Palladium Nanodots
396 for Enhanced Electrocatalytic Carbon Dioxide Reduction. *Chem. Asian J.* 13, 2800{
397 2804, DOI: 10.1002/asia.201800946 , (2018).
- 398 (28) Guo, S.; Zhang, Y.; Zhang, X.; Easton, C. D.; MacFarlane, D. R.; Zhang, J. Phos-
399 phomolybdic Acid-Assisted Growth of Ultrathin Bismuth Nanosheets for Enhanced
400 Electrocatalytic Reduction of CO₂ to Formate. *ChemSusChem* 12, 1091{1100, DOI:
401 10.1002/cssc.201802409 , (2019).

- 402 (29) Raciti, D.; Wang, Y.; Park, J. H.; Wang, C. Three-Dimensional Hierarchical Copper-
403 Based Nanostructures as Advanced Electrocatalysts for CO₂ Reduction. ACS Appl.
404 Energy Mater. 1, 2392{2398, DOI:10.1021/acsaem.8b00356 (2018).
- 405 (30) Kau man, D. R.; Alfonso, D. R.; Tafen, D. N.; Wang, C.; Zhou, Y.; Yu, Y.;
406 Lekse, J. W.; Deng, X.; Espinoza, V.; Trindell, J.; Ranasingha, O. K.; Roy, A.;
407 Lee, J.-S.; Xin, H. L. Selective Electrocatalytic Reduction of CO₂ into CO at
408 Small, Thiol-Capped Au/Cu Nanoparticles. J. Phys. Chem. C 12227991{28000, DOI:
409 10.1021/acs.jpcc.8b06234 , (2018).
- 410 (31) Bejtka, K.; Zeng, J.; Sacco, A.; Castellino, M.; Hernandez, S.; Farkhondehfar, M. A.;
411 Savino, U.; Ansaloni, S.; Pirri, C. F.; Chiodoni, A. Chainlike Mesoporous SnO₂ as
412 a Well-Performing Catalyst for Electrochemical CO₂ Reduction. ACS Appl. Energy
413 Mater. 2, 3081{3091, DOI:10.1021/acsaem.8b02048 (2019).
- 414 (32) Liu, H.; Xiang, K.; Liu, Y.; Zhu, F.; Zou, M.; Yan, X.; Chai, L. Polydopamine
415 Functionalized Cu Nanowires for Enhanced CO₂ Electroreduction Towards Methane.
416 ChemElectroChem 53991{3999, DOI:10.1002/celec.201801132 , (2018).
- 417 (33) Duan, Y.-X.; Meng, F.-L.; Liu, K.-H.; Yi, S.-S.; Li, S.-J.; Yan, J.-M.; Jiang, Q. Amor-
418 phizing of Cu Nanoparticles toward Highly Efficient and Robust Electrocatalyst for
419 CO₂ Reduction to Liquid Fuels with High Faradaic Efficiencies. Adv. Mater. 30,
420 1706194, DOI:10.1002/adma.201706194 (2018).
- 421 (34) Lu, Q.; Rosen, J.; Zhou, Y.; Hutchings, G. S.; Kimmel, Y. C.; Chen, J. G.; Jiao, F. A
422 selective and efficient electrocatalyst for carbon dioxide reduction Nat. Commun. 5,
423 3242, DOI:10.1038/ncomms4242(2014).
- 424 (35) Hsieh, Y.-C.; Senanayake, S. D.; Zhang, Y.; Xu, W.; Polyansky, D. E. Effect
425 of Chloride Anions on the Synthesis and Enhanced Catalytic Activity of Silver

- 426 Nanocoral Electrodes for CO₂ Electroreduction. ACS Catal. 5, 5349{5356, DOI:
427 10.1021/acscatal.5b01235 , (2015).
- 428 (36) Cui, X.; Pan, Z.; Zhang, L.; Peng, H.; Zheng, G. Selective Etching of Nitrogen-Doped
429 Carbon by Steam for Enhanced Electrochemical CO₂ Reduction. Adv. Energy Mater.
430 7, 1701456, DOI:10.1002/aenm.201701456 (2017).
- 431 (37) Han, N. et al. Supported Cobalt Polyphthalocyanine for High-Performance Electro-
432 catalytic CO₂ Reduction. Chem 3 652{664, DOI: 10.1016/j.chempr.2017.08.002 ,
433 (2017).
- 434 (38) Li, F.; Chen, L.; Knowles, G. P.; MacFarlane, D. R.; Zhang, J. Hierarchical Mesoporous
435 SnO₂ Nanosheets on Carbon Cloth: A Robust and Flexible Electrocatalyst for CO₂
436 Reduction with High Efficiency and Selectivity. Angew. Chem. Int. Ed. 56 505{509,
437 DOI: 10.1002/anie.201608279 , (2017).
- 438 (39) Pan, F.; Deng, W.; Justiniano, C.; Li, Y. Identification of champion transition met-
439 als centers in metal and nitrogen-codoped carbon catalysts for CO₂ reduction. Appl.
440 Catal. B 226, 463{472, DOI: 10.1016/j.apcatb.2018.01.001 , (2018).
- 441 (40) Li, C. W.; Kanan, M. W. CO₂ Reduction at Low Overpotential on Cu Electrodes
442 Resulting from the Reduction of Thick Cu₂ O Films. J. Am. Chem. Soc. 134 7231{
443 7234, DOI:10.1021/ja3010978 , (2012).
- 444 (41) Lu, P.; Yang, Y.; Yao, J.; Wang, M.; Dipazir, S.; Yuan, M.; Zhang, J.; Wang, X.;
445 Xie, Z.; Zhang, G. Facile synthesis of single-nickel-atomic dispersed N-doped carbon
446 framework for efficient electrochemical CO₂ reduction. Appl. Catal. B 241, 113{119,
447 DOI: 10.1016/j.apcatb.2018.09.025 , (2019).
- 448 (42) Luc, W.; Collins, C.; Wang, S.; Xin, H.; He, K.; Kang, Y.; Jiao, F. Ag{Sn Bimetallic
449 Catalyst with a Core{Shell Structure for CO₂ Reduction. J. Am. Chem. Soc. 139
450 1885{1893, DOI:10.1021/jacs.6b10435 , (2017).

- 451 (43) Rogers, C.; Perkins, W. S.; Veber, G.; Williams, T. E.; Cloke, R. R.; Fischer, F. R.
452 Synergistic Enhancement of Electrocatalytic CO₂ Reduction with Gold Nanoparticles
453 Embedded in Functional Graphene Nanoribbon Composite Electrodes. *J. Am. Chem.*
454 *Soc.* 139 4052{4061, DOI:10.1021/jacs.6b12217 , (2017).
- 455 (44) Cao, Z.; Zacate, S. B.; Sun, X.; Liu, J.; Hale, E. M.; Carson, W. P.; Tyndall, S. B.;
456 Xu, J.; Liu, X.; Liu, X.; Song, C.; Luo, J.-h.; Cheng, M.-J.; Wen, X.; Liu, W. Tuning
457 Gold Nanoparticles with Chelating Ligands for Highly Efficient Electrocatalytic CO₂
458 Reduction. *Angew. Chem.* 13012857{12861, DOI:10.1002/ange.201805696, (2018).
- 459 (45) School of Petrochemical Engineering, Changzhou University, Changzhou 213164,
460 P. R. China.; Bei, J. Efficient Reduction of CO₂ to Formate Using in Situ Pre-
461 pared Nano-Sized Bi Electro-catalyst. *Int. J. Electrochem. Sci.* 2365{2375, DOI:
462 10.20964/2017.03.72 , (2017).
- 463 (46) Su, P.; Xu, W.; Qiu, Y.; Zhang, T.; Li, X.; Zhang, H. Ultrathin Bismuth Nanosheets
464 as a Highly Efficient CO₂ Reduction Electrocatalyst. *ChemSusChem* 1,1848{853,
465 DOI: 10.1002/cssc.201702229 , (2018).
- 466 (47) Yang, H.; Han, N.; Deng, J.; Wu, J.; Wang, Y.; Hu, Y.; Ding, P.; Li, Y.; Li, Y.; Lu, J.
467 Selective CO₂ Reduction on 2D Mesoporous Bi Nanosheets. *Adv. Energy Mater.* 8
468 1801536, DOI:10.1002/aenm.201801536 (2018).
- 469 (48) Han, P.; Yu, X.; Yuan, D.; Kuang, M.; Wang, Y.; Al-Enizi, A. M.; Zheng, G. Defective
470 graphene for electrocatalytic CO₂ reduction. *J. Colloid Interface Sci.* 534 332{337,
471 DOI: 10.1016/j.jcis.2018.09.036 , (2019).
- 472 (49) Zheng, X.; Han, J.; Fu, Y.; Deng, Y.; Liu, Y.; Yang, Y.; Wang, T.; Zhang, L. Highly
473 efficient CO₂ reduction on ordered porous Cu electrode derived from Cu₂O inverse
474 opals. *Nano Energy* 48 93{100, DOI: 10.1016/j.nanoen.2018.03.023 , (2018).

- 475 (50) Jiang, B.; Zhang, X.-G.; Jiang, K.; Wu, D.-Y.; Cai, W.-B. Boosting Formate Produc-
476 tion in Electrocatalytic CO₂ Reduction over Wide Potential Window on Pd Surfaces.
477 J. Am. Chem. Soc. 1402880{2889, DOI:10.1021/jacs.7b12506 , (2018).
- 478 (51) Rosen, J.; Hutchings, G. S.; Lu, Q.; Forest, R. V.; Moore, A.; Jiao, F. Electrodeposited
479 Zn Dendrites with Enhanced CO Selectivity for Electrocatalytic CO₂ Reduction. ACS
480 Catal. 5, 4586{4591, DOI:10.1021/acscatal.5b00922 , (2015).
- 481 (52) Jiang, K.; Wang, H.; Cai, W.-B.; Wang, H. Li Electrochemical Tuning of Metal
482 Oxide for Highly Selective CO₂ Reduction. ACS Nano 11, 6451{6458, DOI:
483 10.1021/acsnano.7b03029, (2017).
- 484 (53) Cho, M.; Song, J. T.; Back, S.; Jung, Y.; Oh, J. The Role of Adsorbed CN and Cl on
485 an Au Electrode for Electrochemical CO₂ Reduction. ACS Catal. 8, 1178{1185, DOI:
486 10.1021/acscatal.7b03449 , (2018).
- 487 (54) Lv, W.; Zhou, J.; Bei, J.; Zhang, R.; Wang, L.; Xu, Q.; Wang, W. Electrodeposition of
488 nano-sized bismuth on copper foil as electrocatalyst for reduction of CO₂ to formate.
489 Appl. Surf. Sci. 393 191{196, DOI: 10.1016/j.apsusc.2016.10.017 , (2017).
- 490 (55) Xie, J.; Zhao, X.; Wu, M.; Li, Q.; Wang, Y.; Yao, J. Metal-Free Fluorine-Doped Car-
491 bon Electrocatalyst for CO₂ Reduction Outcompeting Hydrogen Evolution. Angew.
492 Chem. Int. Ed. 57, 9640{9644, DOI:10.1002/anie.201802055 , (2018).
- 493 (56) Pan, F.; Zhao, H.; Deng, W.; Feng, X.; Li, Y. A novel N,Fe-Decorated carbon nan-
494 otube/carbon nanosheet architecture for efficient CO₂ reduction. Electrochim. Acta
495 273, 154{161, DOI: 10.1016/j.electacta.2018.04.047 , (2018).
- 496 (57) Kornienko, N.; Zhao, Y.; Kley, C. S.; Zhu, C.; Kim, D.; Lin, S.; Chang, C. J.;
497 Yaghi, O. M.; Yang, P. Metal{Organic Frameworks for Electrocatalytic Reduction of
498 Carbon Dioxide. J. Am. Chem. Soc. 13714129{14135, DOI:10.1021/jacs.5b08212 ,
499 (2015).

- 500 (58) Yang, H.; Wu, Y.; Lin, Q.; Fan, L.; Chai, X.; Zhang, Q.; Liu, J.; He, C.; Lin, Z. Com-
501 position Tailoring via N and S Co-doping and Structure Tuning by Constructing Hier-
502 archical Pores: Metal-Free Catalysts for High-Performance Electrochemical Reduction
503 of CO₂. *Angew. Chem. Int. Ed.* 57 15476{15480, DOI:10.1002/anie.201809255 ,
504 (2018).
- 505 (59) Geng, Z.; Kong, X.; Chen, W.; Su, H.; Liu, Y.; Cai, F.; Wang, G.; Zeng, J. Oxy-
506 gen Vacancies in ZnO Nanosheets Enhance CO₂ Electrochemical Reduction to CO.
507 *Angew. Chem. Int. Ed.* 57 6054{6059, DOI:10.1002/anie.201711255 , (2018).
- 508 (60) Zhang, W.; Hu, Y.; Ma, L.; Zhu, G.; Zhao, P.; Xue, X.; Chen, R.; Yang, S.; Ma, J.;
509 Liu, J.; Jin, Z. Liquid-phase exfoliated ultrathin Bi nanosheets: Uncovering the origins
510 of enhanced electrocatalytic CO₂ reduction on two-dimensional metal nanostructure.
511 *Nano Energy* 53 808{816, DOI: 10.1016/j.nanoen.2018.09.053 , (2018).
- 512 (61) Cao, Z.; Derrick, J. S.; Xu, J.; Gao, R.; Gong, M.; Nichols, E. M.; Smith, P. T.;
513 Liu, X.; Wen, X.; Copèret, C.; Chang, C. J. Chelating N-Heterocyclic Carbene Ligands
514 Enable Tuning of Electrocatalytic CO₂ Reduction to Formate and Carbon Monox-
515 ide: Surface Organometallic Chemistry *Angew. Chem. Int. Ed.* 57 4981{4985, DOI:
516 10.1002/anie.201800367 , (2018).
- 517 (62) Zhao, C.; Wang, J. Electrochemical reduction of CO₂ to formate in aqueous
518 solution using electro-deposited Sn catalysts *Chem. Eng. J.* 293 161{170, DOI:
519 10.1016/j.cej.2016.02.084 , (2016).
- 520 (63) Zhang, X.; Lei, T.; Liu, Y.; Qiao, J. Enhancing CO₂ electrolysis to formate on
521 facilely synthesized Bi catalysts at low overpotential *Appl. Catal. B* 218 46{50, DOI:
522 10.1016/j.apcatb.2017.06.032 , (2017).
- 523 (64) He, J.; Liu, X.; Liu, H.; Zhao, Z.; Ding, Y.; Luo, J. Highly selective electrocatalytic

- 524 reduction of CO₂ to formate over Tin(IV) sul de monolayers.J. Catal. 364, 125{130,
525 DOI: 10.1016/j.jcat.2018.05.005 , (2018).
- 526 (65) Smith, P. T.; Benke, B. P.; Cao, Z.; Kim, Y.; Nichols, E. M.; Kim, K.; Chang, C. J.
527 Iron Porphyrins Embedded into a Supramolecular Porous Organic Cage for Electro-
528 chemical CO₂ Reduction in Water. Angew. Chem. Int. Ed. 57 9684{9688, DOI:
529 10.1002/anie.201803873 , (2018).
- 530 (66) Zhang, A.; He, R.; Li, H.; Chen, Y.; Kong, T.; Li, K.; Ju, H.; Zhu, J.; Zhu, W.;
531 Zeng, J. Nickel Doping in Atomically Thin Tin Disul de Nanosheets Enables
532 Highly E cient CO₂ Reduction. Angew. Chem. Int. Ed. 57 10954{10958, DOI:
533 10.1002/anie.201806043 , (2018).
- 534 (67) Morimoto, M.; Takatsuji, Y.; Hirata, K.; Fukuma, T.; Ohno, T.; Sakakura, T.;
535 Haruyama, T. Visualization of catalytic edge reactivity in electrochemical CO₂
536 reduction on porous Zn electrode.Electrochim. Acta 290 255{261, DOI:
537 10.1016/j.electacta.2018.09.080 , (2018).
- 538 (68) Spataru, N.; Tokuhiko, K.; Terashima, C.; Rao, T. N.; Fujishima, A. Electrochemical
539 reduction of carbon dioxide at ruthenium dioxide deposited on boron-doped diamond.
540 J. Appl. Electrochem. 33 1205{1210, DOI:10.1023/B:JACH.0000003866.85015.b6
541 (2003).
- 542 (69) Hirota, K.; Tryk, D. A.; Yamamoto, T.; Hashimoto, K.; Okawa, M.; Fujishima, A.
543 Photoelectrochemical Reduction of CO₂ in a High-Pressure CO₂ + Methanol
544 Medium at p-Type Semiconductor ElectrodesJ. Phys. Chem. B 102 9834{9843,
545 DOI: 10.1021/jp9822945 , (1998).
- 546 (70) Liu, X.; Yang, H.; He, J.; Liu, H.; Song, L.; Li, L.; Luo, J. Highly Active, Durable
547 Ultrathin MoTe₂ Layers for the Electroreduction of CO₂ to CH₄. Small 14 1704049,
548 DOI: 10.1002/smll.201704049 , (2018).

- 549 (71) Li, F.; Chen, L.; Xue, M.; Williams, T.; Zhang, Y.; MacFarlane, D. R.; Zhang, J.
550 Towards a better Sn: Efficient electrocatalytic reduction of CO₂ to formate
551 by Sn/SnS₂ derived from SnS₂ nanosheets. *Nano Energy* 31 270{277, DOI:
552 10.1016/j.nanoen.2016.11.004 , (2017).
- 553 (72) Hu, X.-M.; Rønne, M. H.; Pedersen, S. U.; Skrydstrup, T.; Daasbjerg, K. En-
554 hanced Catalytic Activity of Cobalt Porphyrin in CO₂ Electroreduction upon Im-
555 mobilization on Carbon Materials. *Angew. Chem. Int. Ed.* 56 6468{6472, DOI:
556 10.1002/anie.201701104 , (2017).
- 557 (73) Liu, S.; Tao, H.; Zeng, L.; Liu, Q.; Xu, Z.; Liu, Q.; Luo, J.-L. Shape-Dependent
558 Electrocatalytic Reduction of CO₂ to CO on Triangular Silver Nanoplates. *J. Am.*
559 *Chem. Soc.* 1392160{2163, DOI:10.1021/jacs.6b12103 , (2017).
- 560 (74) Liu, S.; Xiao, J.; Lu, X. F.; Wang, J.; Wang, X.; Lou, X. W. D. Efficient Elec-
561 trochemical Reduction of CO₂ to HCOOH over Sub-2 nm SnO₂ Quantum Wires
562 with Exposed Grain Boundaries. *Angew. Chem. Int. Ed.* 58 8499{8503, DOI:
563 10.1002/anie.201903613 , (2019).
- 564 (75) Liu, S.; Yang, H.; Huang, X.; Liu, L.; Cai, W.; Gao, J.; Li, X.; Zhang, T.; Huang, Y.;
565 Liu, B. Identifying Active Sites of Nitrogen-Doped Carbon Materials for the CO₂ Re-
566 duction Reaction. *Adv. Funct. Mater.* 28, 1800499, DOI:10.1002/adfm.201800499,
567 (2018).
- 568 (76) Nursanto, E. B.; Jeon, H. S.; Kim, C.; Jee, M. S.; Koh, J. H.; Hwang, Y. J.; Min, B. K.
569 Gold catalyst reactivity for CO₂ electro-reduction: From nano particle to layer. *Catal.*
570 *Today* 260 107{111, DOI: 10.1016/j.cattod.2015.05.017 , (2016).
- 571 (77) Peng, X.; Karakalos, S. G.; Mustain, W. E. Preferentially Oriented Ag Nanocrys-
572 tals with Extremely High Activity and Faradaic Efficiency for CO₂ Electro-

- 573 chemical Reduction to CO. ACS Appl. Mater. Interfaces 10 1734{1742, DOI:
574 10.1021/acsami.7b16164, (2018).
- 575 (78) Zhu, W.; Zhang, L.; Yang, P.; Chang, X.; Dong, H.; Li, A.; Hu, C.; Huang, Z.;
576 Zhao, Z.-J.; Gong, J. Morphological and Compositional Design of Pd-Cu Bimetallic
577 Nanocatalysts with Controllable Product Selectivity toward CO₂ Electroreduction.
578 Small 14 1703314, DOI:10.1002/smll.201703314 , (2018).
- 579 (79) Geng, Z.; Cao, Y.; Chen, W.; Kong, X.; Liu, Y.; Yao, T.; Lin, Y. Regulating the coordi-
580 nation environment of Co single atoms for achieving efficient electrocatalytic activity in
581 CO₂ reduction. Appl. Catal. B 240 234{240, DOI:10.1016/j.apcatb.2018.08.075 ,
582 (2019).
- 583 (80) Kim, D.; Kley, C. S.; Li, Y.; Yang, P. Copper nanoparticle ensembles for selective
584 electroreduction of CO₂ to C₂{C₃ products. Proc. Natl. Acad. Sci. 114 10560{
585 10565, DOI:10.1073/pnas.1711493114, (2017).
- 586 (81) Chen, Z.; Mou, K.; Yao, S.; Liu, L. Zinc-Coordinated Nitrogen-Codoped Graphene as
587 an Efficient Catalyst for Selective Electrochemical Reduction of CO₂ to CO. Chem-
588 SusChem 1,12944{2952, DOI:10.1002/cssc.201800925 , (2018).
- 589 (82) Kim, S. K.; Zhang, Y.-J.; Bergstrom, H.; Michalsky, R.; Peterson, A. Understanding
590 the Low-Overpotential Production of CH₄ from CO₂ on Mo₂C Catalysts. ACS
591 Catal. 6, 2003{2013, DOI:10.1021/acscatal.5b02424 , (2016).
- 592 (83) Zhu, M.; Ye, R.; Jin, K.; Lazouski, N.; Manthiram, K. Elucidating the Reactivity and
593 Mechanism of CO₂ Electroreduction at Highly Dispersed Cobalt Phthalocyanine ACS
594 Energy Lett. 3, 1381{1386, DOI:10.1021/acsenergylett.8b00519 , (2018).
- 595 (84) Kumar, B.; Atla, V.; Brian, J. P.; Kumari, S.; Nguyen, T. Q.; Sunkara, M.; Spur-
596 geon, J. M. Reduced SnQ Porous Nanowires with a High Density of Grain Boundaries

- 597 as Catalysts for Efficient Electrochemical CO₂-into-HCOOH Conversion. *Angew.*
598 *Chem. Int. Ed.* 56, 3645{3649, DOI:10.1002/anie.201612194 , (2017).
- 599 (85) Wang, H.; Jia, J.; Song, P.; Wang, Q.; Li, D.; Min, S.; Qian, C.; Wang, L.; Li, Y. F.;
600 Ma, C.; Wu, T.; Yuan, J.; Antonietti, M.; Ozin, G. A. Efficient Electrocatalytic Reduc-
601 tion of CO₂ by Nitrogen-Doped Nanoporous Carbon/Carbon Nanotube Membranes:
602 A Step Towards the Electrochemical CO₂ Re nery. *Angew. Chem. Int. Ed.* 56 7847{
603 7852, DOI: 10.1002/anie.201703720 , (2017).
- 604 (86) Wu, J.; Liu, M.; Sharma, P. P.; Yadav, R. M.; Ma, L.; Yang, Y.; Zou, X.; Zhou, X.-D.;
605 Vajtai, R.; Yakobson, B. I.; Lou, J.; Ajayan, P. M. Incorporation of Nitrogen Defects
606 for Efficient Reduction of CO₂ via Two-Electron Pathway on Three-Dimensional
607 Graphene Foam. *Nano Lett.* 16, 466{470, DOI: 10.1021/acs.nanolett.5b04123 ,
608 (2016).
- 609 (87) Ren, W.; Tan, X.; Yang, W.; Jia, C.; Xu, S.; Wang, K.; Smith, S. C.; Zhao, C. Isolated
610 Diatomic Ni-Fe Metal{Nitrogen Sites for Synergistic Electroreduction of CO₂. *Angew.*
611 *Chem. Int. Ed.* 58, 6972{6976, DOI:10.1002/anie.201901575 , (2019).
- 612 (88) Li, L.; Ma, D.-K.; Qi, F.; Chen, W.; Huang, S. Bi nanoparticles/Bi₂O₃ nanosheets with
613 abundant grain boundaries for efficient electrocatalytic CO₂ reduction. *Electrochim.*
614 *Acta* 298, 580{586, DOI: 10.1016/j.electacta.2018.12.116 , (2019).
- 615 (89) Hu, X.-M.; Hval, H. H.; Bjerglund, E. T.; Dalgaard, K. J.; Madsen, M. R.; Pohl, M.-
616 M.; Welter, E.; Lamagni, P.; Buhl, K. B.; Bremholm, M.; Beller, M.; Pedersen, S. U.;
617 Skrydstrup, T.; Daasbjerg, K. Selective CO₂ Reduction to CO in Water using Earth-
618 Abundant Metal and Nitrogen-Doped Carbon Electrocatalysts *ACS Catal.* 8, 6255{
619 6264, DOI: 10.1021/acscatal.8b01022 , (2018).
- 620 (90) Zhang, L.; Wu, N.; Zhang, J.; Hu, Y.; Wang, Z.; Zhuang, L.; Jin, X. Imidazolium

- 621 Ions with an Alcohol Substituent for Enhanced Electrocatalytic Reduction of CO₂.
622 ChemSusChem 1,04824{4828, DOI:10.1002/cssc.201701673, (2017).
- 623 (91) Liu, K.; Wang, J.; Shi, M.; Yan, J.; Jiang, Q. Simultaneous Achieving of High Faradaic
624 Efficiency and CO Partial Current Density for CO₂ Reduction via Robust, Noble-
625 Metal-Free Zn Nanosheets with Favorable Adsorption Energy Adv. Energy Mater. 9
626 1900276, DOI:10.1002/aenm.201900276 (2019).
- 627 (92) Zhu, W.; Zhang, L.; Yang, P.; Hu, C.; Dong, H.; Zhao, Z.-J.; Mu, R.; Gong, J. Forma-
628 tion of Enriched Vacancies for Enhanced CO₂ Electrocatalytic Reduction over AuCu
629 Alloys. ACS Energy Lett. 3 2144{2149, DOI: 10.1021/acsenergylett.8b01286 ,
630 (2018).
- 631 (93) Sun, X.; Lu, L.; Zhu, Q.; Wu, C.; Yang, D.; Chen, C.; Han, B. MoP Nanoparti-
632 cles Supported on Indium-Doped Porous Carbon: Outstanding Catalysts for Highly
633 Efficient CO₂ Electroreduction. Angew. Chem. Int. Ed. 57 2427{2431, DOI:
634 10.1002/anie.201712221 , (2018).
- 635 (94) Ghausi, M. A.; Xie, J.; Li, Q.; Wang, X.; Yang, R.; Wu, M.; Wang, Y.; Dai, L. CO
636 ₂ Overall Splitting by a Bifunctional Metal-Free Electrocatalyst. Angew. Chem. Int.
637 Ed. 57, 13135{13139, DOI:10.1002/anie.201807571 , (2018).
- 638 (95) Verma, S.; Hamasaki, Y.; Kim, C.; Huang, W.; Lu, S.; Jhong, H.-R. M.;
639 Gewirth, A. A.; Fujigaya, T.; Nakashima, N.; Kenis, P. J. A. Insights into
640 the Low Overpotential Electroreduction of CO₂ to CO on a Supported Gold
641 Catalyst in an Alkaline Flow Electrolyzer. ACS Energy Lett. 3 193{198, DOI:
642 10.1021/acsenergylett.7b01096 , (2018).
- 643 (96) Hsieh, Y.-C.; Betancourt, L. E.; Senanayake, S. D.; Hu, E.; Zhang, Y.; Xu, W.;
644 Polyansky, D. E. Modification of CO₂ Reduction Activity of Nanostructured Silver

- 645 Electrochemical Catalysts by Surface Halide Anions ACS Appl. Energy Mater. 2, 102{109, DOI:
646 10.1021/acsaem.8b01692 (2019).
- 647 (97) Ma, M.; Djanashvili, K.; Smith, W. A. Selective electrochemical reduction of CO₂ to
648 CO on CuO-derived Cu nanowires Phys. Chem. Chem. Phys. 17, 20861{20867, DOI:
649 10.1039/C5CP03559G (2015).
- 650 (98) Gu, J.; Hsu, C.-S.; Bai, L.; Chen, H. M.; Hu, X. Atomically dispersed Fe³⁺
651 sites catalyze efficient CO₂ electroreduction to CO. Science 364, 1091{1094, DOI:
652 10.1126/science.aaw7515 , (2019).
- 653 (99) Miao, C.-C.; Yuan, G.-Q. Morphology-Controlled Bi₂ O₃ Nanoparticles as Catalysts
654 for Selective Electrochemical Reduction of CO₂ to Formate. ChemElectroChem 5
655 3741{3747, DOI:10.1002/celec.201801036 , (2018).
- 656 (100) He, R.; Zhang, A.; Ding, Y.; Kong, T.; Xiao, Q.; Li, H.; Liu, Y.; Zeng, J. Achieving
657 the Widest Range of Syngas Proportions at High Current Density over Cadmium
658 Sulfoselenide Nanorods in CO₂ Electroreduction. Adv. Mater. 30, 1705872, DOI:
659 10.1002/adma.201705872 (2018).
- 660 (101) Todoroki, N.; Tei, H.; Tsurumaki, H.; Miyakawa, T.; Inoue, T.; Wadayama, T. Surface
661 Atomic Arrangement Dependence of Electrochemical CO₂ Reduction on Gold: Online
662 Electrochemical Mass Spectrometric Study on Low-Index Au(hkl) Surfaces. ACS
663 Catal. 9, 1383{1388, DOI:10.1021/acscatal.8b04852 , (2019).
- 664 (102) Huang, J.; Guo, X.; Wei, Y.; Hu, Q.; Yu, X.; Wang, L. A renewable, flexible and
665 robust single layer nitrogen-doped graphene coating Sn foil for boosting formate
666 production from electrocatalytic CO₂ reduction. J. CO₂ Util. 33, 166{170, DOI:
667 10.1016/j.jcou.2019.05.026 , (2019).
- 668 (103) He, S.; Ni, F.; Ji, Y.; Wang, L.; Wen, Y.; Bai, H.; Liu, G.; Zhang, Y.; Li, Y.; Zhang, B.;

- 669 Peng, H. The p-Orbital Delocalization of Main-Group Metals to Boost CO₂ Electrore-
670 duction. *Angew. Chem.* 13016346{16351, DOI:10.1002/ange.201810538, (2018).
- 671 (104) Zhao, C. et al. Solid-Diffusion Synthesis of Single-Atom Catalysts Directly
672 from Bulk Metal for Efficient CO₂ Reduction. *Joule* 3, 584{594, DOI:
673 10.1016/j.joule.2018.11.008, (2019).
- 674 (105) Vasile, A.; Zheng, Y.; Qiao, S. Z. Carbon Solving Carbon's Problems: Recent
675 Progress of Nanostructured Carbon-Based Catalysts for the Electrochemical Reduc-
676 tion of CO₂. *Adv. Energy Mater.* 7, 1700759, DOI:10.1002/aenm.201700759 (2017).
- 677 (106) Xia, Z.; Freeman, M.; Zhang, D.; Yang, B.; Lei, L.; Li, Z.; Hou, Y. Highly Selective
678 Electrochemical Conversion of CO₂ to HCOOH on Dendritic Indium Foams. *Chem-*
679 *ElectroChem* 5 253{259, DOI: 10.1002/celc.201700935, (2018).
- 680 (107) Zhu, M.; Chen, J.; Guo, R.; Xu, J.; Fang, X.; Han, Y.-F. Cobalt phthalocyanine
681 coordinated to pyridine-functionalized carbon nanotubes with enhanced CO₂ elec-
682 troreduction. *Appl. Catal. B* 251, 112{118, DOI: 10.1016/j.apcatb.2019.03.047, ,
683 (2019).
- 684 (108) Liu, S.; Yang, H. B.; Hung, S.; Ding, J.; Cai, W.; Liu, L.; Gao, J.; Li, X.; Ren, X.;
685 Kuang, Z.; Huang, Y.; Zhang, T.; Liu, B. Elucidating the Electrocatalytic CO₂
686 Reduction Reaction over a Model Single-Atom Nickel Catalyst *Angew. Chem. Int.*
687 *Ed.* 59, 798{803, DOI: 10.1002/anie.201911995, (2020).
- 688 (109) Zhao, Y.; Liang, J.; Wang, C.; Ma, J.; Wallace, G. G. Tunable and Efficient Tin
689 Modified Nitrogen-Doped Carbon Nanofibers for Electrochemical Reduction of Aque-
690 ous Carbon Dioxide. *Adv. Energy Mater.* 8 1702524, DOI:10.1002/aenm.201702524
691 (2018).
- 692 (110) Chang, X.; Wang, T.; Zhao, Z.; Yang, P.; Greeley, J.; Mu, R.; Zhang, G.; Gong, Z.;
693 Luo, Z.; Chen, J.; Cui, Y.; Ozin, G. A.; Gong, J. Tuning Cu/Cu₂O Interfaces for the

- 694 Reduction of Carbon Dioxide to Methanol in Aqueous Solutions *Angew. Chem.* 130
695 15641{15645, DOI:10.1002/ange.201805256, (2018).
- 696 (111) Song, J. T.; Ryoo, H.; Cho, M.; Kim, J.; Kim, J.-G.; Chung, S.-Y.; Oh, J. Nanoporous
697 Au Thin Films on Si Photoelectrodes for Selective and Efficient Photoelectrochemical
698 CO₂ Reduction. *Adv. Energy Mater.* 7, 1601103, DOI:10.1002/aenm.201601103
699 (2017).
- 700 (112) Liu, X.; Schlexer, P.; Xiao, J.; Ji, Y.; Wang, L.; Sandberg, R. B.; Tang, M.;
701 Brown, K. S.; Peng, H.; Ringe, S.; Hahn, C.; Jaramillo, T. F.; Nørskov, J. K.; Chan, K.
702 pH effects on the electrochemical reduction of CO₂ towards C₂ products on stepped
703 copper. *Nat. Commun.* 10 32, DOI: 10.1038/s41467-018-07970-9, (2019).
- 704 (113) Huang, P.; Cheng, M.; Zhang, H.; Zuo, M.; Xiao, C.; Xie, Y. Single Mo atom realized
705 enhanced CO₂ electro-reduction into formate on N-doped graphene. *Nano Energy* 61
706 428{434, DOI: 10.1016/j.nanoen.2019.05.003, (2019).
- 707 (114) Sun, K.; Wu, L.; Qin, W.; Zhou, J.; Hu, Y.; Jiang, Z.; Shen, B.; Wang, Z. Enhanced
708 electrochemical reduction of CO₂ to CO on Ag electrocatalysts with increased unoccu-
709 pied density of states. *J. Mater. Chem. A* 4, 12616{12623, DOI:10.1039/C6TA04325A
710 (2016).
- 711 (115) Wu, H.; Zeng, M.; Zhu, X.; Tian, C.; Mei, B.; Song, Y.; Du, X.-L.; Jiang, Z.; He, L.;
712 Xia, C.; Dai, S. Defect Engineering in Polymeric Cobalt Phthalocyanine Networks for
713 Enhanced Electrochemical CO₂ Reduction. *ChemElectroChem* 5 2717{2721, DOI:
714 10.1002/celec.201800806, (2018).
- 715 (116) Yang, F.; Song, P.; Liu, X.; Mei, B.; Xing, W.; Jiang, Z.; Gu, L.; Xu, W. Highly
716 Efficient CO₂ Electroreduction on ZnN₄-based Single-Atom Catalyst. *Angew. Chem.*
717 *Int. Ed.* 57, 12303{12307, DOI:10.1002/anie.201805871, (2018).

- 718 (117) Choi, J.; Benedetti, T. M.; Jalili, R.; Walker, A.; Wallace, G. G.; O'cer, D. L.
719 High Performance Fe Porphyrin/Ionic Liquid Co-catalyst for Electrochemical CO₂
720 Reduction. *Chem. Eur. J.* 22, 14158{14161, DOI:10.1002/chem.201603359 (2016).
- 721 (118) Fan, Q.; Hou, P.; Choi, C.; Wu, T.; Hong, S.; Li, F.; Soo, Y.; Kang, P.; Jung, Y.;
722 Sun, Z. Activation of Ni Particles into Single Ni_N Atoms for Efficient Electrochemical
723 Reduction of CO₂. *Adv. Energy Mater.* 10, 1903068, DOI:10.1002/aenm.201903068
724 (2020).
- 725 (119) Zhang, L.; Wang, Z.; Mehio, N.; Jin, X.; Dai, S. Thickness- and Particle-Size-
726 Dependent Electrochemical Reduction of Carbon Dioxide on Thin-Layer Porous Silver
727 Electrodes. *ChemSusChem*, 9, 428{432, DOI: 10.1002/cssc.201501637, (2016).
- 728 (120) Han, J.; An, P.; Liu, S.; Zhang, X.; Wang, D.; Yuan, Y.; Guo, J.; Qiu, X.; Hou, K.;
729 Shi, L.; Zhang, Y.; Zhao, S.; Long, C.; Tang, Z. Reordering of Orbital Energies of
730 Single-Site Catalysts for CO₂ Electroreduction. *Angew. Chem. Int. Ed.* 58, 12711{
731 12716, DOI:10.1002/anie.201907399, (2019).
- 732 (121) Hu, H.; Gui, L.; Zhou, W.; Sun, J.; Xu, J.; Wang, Q.; He, B.; Zhao, L. Partially
733 reduced Sn/SnO₂ porous hollow fiber: A highly selective, efficient and robust elec-
734 trocatalyst towards carbon dioxide reduction. *Electrochim. Acta* 285, 70{77, DOI:
735 10.1016/j.electacta.2018.08.002, (2018).
- 736 (122) Koh, J. H.; Jeon, H. S.; Jee, M. S.; Nursanto, E. B.; Lee, H.; Hwang, Y. J.; Min, B. K.
737 Oxygen Plasma Induced Hierarchically Structured Gold Electrocatalyst for Selective
738 Reduction of Carbon Dioxide to Carbon Monoxide. *J. Phys. Chem. C* 119, 883{889,
739 DOI: 10.1021/jp509967m, (2015).
- 740 (123) Shen, Q.; Chen, Z.; Huang, X.; Liu, M.; Zhao, G. High-Yield and Selective Photoelec-
741 trocatalytic Reduction of CO₂ to Formate by Metallic Copper Decorated Co₃O₄

- 742 Nanotube Arrays. *Env. Sci. Tech.* 49 5828{5835, DOI:10.1021/acs.est.5b00066 ,
743 (2015).
- 744 (124) Morlares, N.; Takanebe, K.; Rodionov, V. Simultaneous Reduction of CO₂ and Split-
745 ting of H₂O by a Single Immobilized Cobalt Phthalocyanine Electrocatalyst *ACS*
746 *Catal.* 6, 3092{3095, DOI:10.1021/acscatal.6b00543 , (2016).
- 747 (125) Liu, M. et al. Quantum-Dot-Derived Catalysts for CO₂ Reduction Reaction *Joule* 3
748 1703{1718, DOI:10.1016/j.joule.2019.05.010 , (2019).
- 749 (126) Xiang, H.; Rasul, S.; Scott, K.; Portoles, J.; Cumpson, P.; Yu, E. H. Enhanced se-
750 lectivity of carbonaceous products from electrochemical reduction of CO₂ in aqueous
751 media. *J. CO₂ Util.* 30, 214{221, DOI: 10.1016/j.jcou.2019.02.007 , (2019).
- 752 (127) Han, H.; Park, S.; Jang, D.; Lee, S.; Kim, W. B. Electrochemical Reduction of CO₂
753 to CO by N,S Dual-Doped Carbon Nanoweb Catalysts *ChemSusChem* 13 539{547,
754 DOI: 10.1002/cssc.201903117 , (2020).
- 755 (128) Jeong, H.; Balamurugan, M.; Choutipalli, V. S. K.; Jo, J.; Baik, H.; Subramanian, V.;
756 Kim, M.; Sim, U.; Nam, K. T. Tris(2-benzimidazolylmethyl)amine-Directed Synthesis
757 of Single-Atom Nickel Catalysts for Electrochemical CO Production from CO₂. *Chem.*
758 *Eur. J.* 24, 18444{18454, DOI:10.1002/chem.201803615 (2018).
- 759 (129) Hu, X.; Yang, H.; Guo, M.; Gao, M.; Zhang, E.; Tian, H.; Liang, Z.; Liu, X. Synthe-
760 sis and Characterization of (Cu, S) Co-doped SnO₂ for Electrocatalytic Reduction
761 of CO₂ to Formate at Low Overpotential. *ChemElectroChem* 5 1330{1335, DOI:
762 10.1002/celec.201800104 , (2018).
- 763 (130) Zhang, X.; Sun, X.; Guo, S.-X.; Bond, A. M.; Zhang, J. Formation of lattice-
764 dislocated bismuth nanowires on copper foam for enhanced electrocatalytic CO₂ re-
765 duction at low overpotential. *Energy & Environmental Science* 12 1334{1340, DOI:
766 10.1039/C9EE00018F(2019).

- 767 (131) Zheng, T.; Jiang, K.; Ta, N.; Hu, Y.; Zeng, J.; Liu, J.; Wang, H. Large-Scale and Highly
768 Selective CO₂ Electrocatalytic Reduction on Nickel Single-Atom Catalyst. *Joule* 3
769 265{278, DOI: 10.1016/j.joule.2018.10.015 , (2019).
- 770 (132) Todoroki, N.; Tei, H.; Miyakawa, T.; Tsurumaki, H.; Wadayama, T. Electrochem-
771 ical CO₂ Reduction on Bimetallic Surface Alloys: Enhanced Selectivity to CO
772 for Co/Au(110) and to H₂ for Sn/Au(110). *ChemElectroChem* 6 3101{3107, DOI:
773 10.1002/celec.201900725 , (2019).
- 774 (133) Gao, S.; Sun, Z.; Liu, W.; Jiao, X.; Zu, X.; Hu, Q.; Sun, Y.; Yao, T.; Zhang, W.;
775 Wei, S.; Xie, Y. Atomic layer connected vacancies for atomic-level insights into car-
776 bon dioxide electroreduction. *Nat. Commun.* 8 14503, DOI:10.1038/ncomms14503
777 (2017).
- 778 (134) Yang, H.-J.; Dong, J.; Hong, Y.-H.; Lin, W.-F.; Zhou, Z.-Y.; Sun, S.-G. Compara-
779 tive investigation of CO₂ and oxygen reduction on Fe/N/C catalysts. *Electrochem.*
780 *Commun.* 97, 82{86, DOI: 10.1016/j.elecom.2018.10.014 , (2018).
- 781 (135) Wang, J.; Gan, L.; Zhang, Q.; Reddu, V.; Peng, Y.; Liu, Z.; Xia, X.; Wang, C.;
782 Wang, X. A Water-Soluble Cu Complex as Molecular Catalyst for Electrocatalytic
783 CO₂ Reduction on Graphene-Based Electrode. *Adv. Energy Mater.* 9 1803151, DOI:
784 10.1002/aenm.201803151 (2019).
- 785 (136) Wang, X.; Xiao, W.; Zhang, J.; Wang, Z.; Jin, X. Nanoporous Ag-Sn derived from
786 codeposited AgCl-SnO₂ for the electrocatalytic reduction of CO₂ with high formate se-
787 lectivity. *Electrochem. Commun.* 10252{56, DOI: 10.1016/j.elecom.2019.03.017 ,
788 (2019).
- 789 (137) Zhang, Q.; Zhang, Y.; Mao, J.; Liu, J.; Zhou, Y.; Guay, D.; Qiao, J. Electrochem-
790 ical Reduction of CO₂ by SnO_x Nanosheets Anchored on Multiwalled Carbon

- 791 Nanotubes with Tunable Functional Groups. *ChemSusChem* 12, 1443–1450, DOI:
792 10.1002/cssc.201802725, (2019).
- 793 (138) Rabiee, A.; Nematollahi, D. Electrochemical reduction of CO₂ to formate ion using
794 nanocubic mesoporous In(OH)₃/carbon black system. *Mater. Chem. Phys.* 193, 109–
795 116, DOI: 10.1016/j.matchemphys.2017.02.016, (2017).
- 796 (139) Lv, K.; Teng, C.; Shi, M.; Yuan, Y.; Zhu, Y.; Wang, J.; Kong, Z.; Lu, X.; Zhu, Y.
797 Hydrophobic and Electronic Properties of the E-MoS₂ Nanosheets Induced by FAS
798 for the CO₂ Electroreduction to Syngas with a Wide Range of CO/H₂ Ratios. *Adv.*
799 *Funct. Mater.* 28, 1802339, DOI:10.1002/adfm.201802339, (2018).
- 800 (140) Min, S.; Yang, X.; Lu, A.-Y.; Tseng, C.-C.; Hedhili, M. N.; Li, L.-J.; Huang, K.-
801 W. Low overpotential and high current CO₂ reduction with surface reconstructed Cu
802 foam electrodes. *Nano Energy* 27, 121–129, DOI: 10.1016/j.nanoen.2016.06.043,
803 (2016).
- 804 (141) Lei, F.; Liu, W.; Sun, Y.; Xu, J.; Liu, K.; Liang, L.; Yao, T.; Pan, B.; Wei, S.; Xie, Y.
805 Metallic tin quantum sheets confined in graphene toward high-efficiency carbon dioxide
806 electroreduction. *Nat. Commun.* 7, 12697, DOI:10.1038/ncomms12697(2016).
- 807 (142) Zhang, M.; Wu, T.-S.; Hong, S.; Fan, Q.; Soo, Y.-L.; Masa, J.; Qiu, J.; Sun, Z. Efficient
808 Electrochemical Reduction of CO₂ by Ni₃N Catalysts with Tunable Performance. *ACS*
809 *Sust. Chem. Eng.* 7, 15030–15035, DOI:10.1021/acssuschemeng.9b03502 (2019).
- 810 (143) Chen, Z.; Mou, K.; Yao, S.; Liu, L. Highly selective electrochemical reduction of CO₂
811 to formate on metal-free nitrogen-doped PC61BM. *Mater. Chem. A* 6, 11236–11243,
812 DOI: 10.1039/C8TA03328E(2018).
- 813 (144) Pan, F.; Liang, A.; Duan, Y.; Liu, Q.; Zhang, J.; Li, Y. Self-growth-templating syn-
814 thesis of 3D N,P,Co-doped mesoporous carbon frameworks for efficient bifunctional

- 815 oxygen and carbon dioxide electroreduction. *J. Mater. Chem. A* *5*, 13104–13111, DOI:
816 10.1039/C7TA03005C, (2017).
- 817 (145) Zhou, J.; Yuan, K.; Zhou, L.; Guo, Y.; Luo, M.; Guo, X.; Meng, Q.; Zhang, Y.
818 Boosting Electrochemical Reduction of CO₂ at a Low Overpotential by Amorphous
819 Ag-Bi-S-O Decorated Bi⁰ Nanocrystals. *Angew. Chem. Int. Ed.* *58*, 14197–14201,
820 DOI: 10.1002/anie.201908735, (2019).
- 821 (146) Kou, W.; Zhang, Y.; Dong, J.; Mu, C.; Xu, L. Nickel–Nitrogen-Doped Three-
822 Dimensional Ordered Macro-/Mesoporous Carbon as an Efficient Electrocatalyst
823 for CO₂ Reduction to CO. *ACS Appl. Energy Mater.* *3*, 1875–1882, DOI:
824 10.1021/acsaem.9b02324, (2020).
- 825 (147) He, S.; Ji, D.; Zhang, J.; Novello, P.; Li, X.; Zhang, Q.; Zhang, X.; Liu, J. Understand-
826 ing the Origin of Selective Reduction of CO₂ to CO on Single-Atom Nickel Catalyst.
827 *J. Phys. Chem. B* *124*, 511–518, DOI: 10.1021/acs.jpcc.9b09730, (2020).
- 828 (148) Wuttig, A.; Yaguchi, M.; Motobayashi, K.; Osawa, M.; Surendranath, Y. Inhibited
829 proton transfer enhances Au-catalyzed CO₂-to-fuels selectivity. *Proc. Natl. Acad. Sci.*
830 *113*, E4585–E4593, (2016).
- 831 (149) Dunwell, M.; Luc, W.; Yan, Y.; Jiao, F.; Xu, B. Understanding surface-mediated elec-
832 trochemical reactions: CO₂ reduction and beyond. *ACS Catal.* *8*, 8121–8129, (2018).
- 833 (150) Williams, K.; Corbin, N.; Zeng, J.; Lazouski, N.; Yang, D.-T.; Manthiram, K. Pro-
834 tecting effect of mass transport during electrochemical reduction of oxygenated carbon
835 dioxide feedstocks. *Sustain. Energy Fuels* *3*, 1225–1232, (2019).